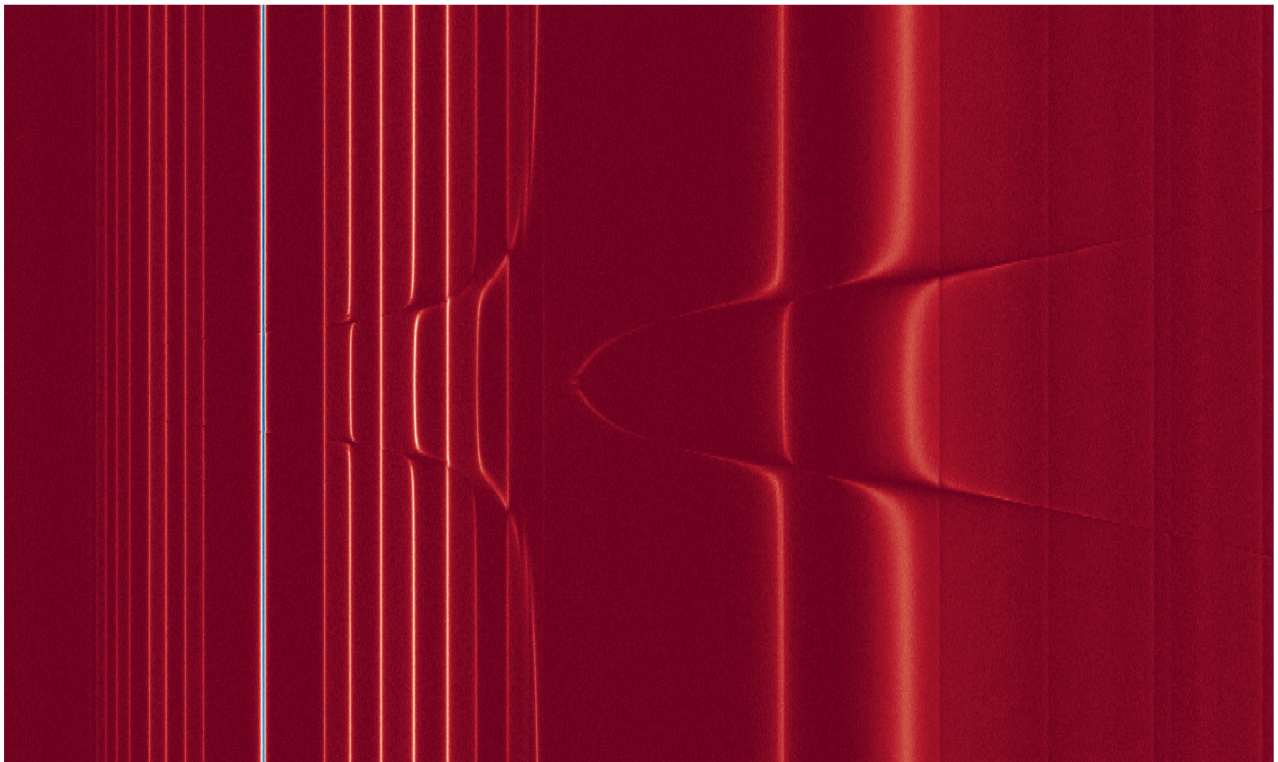


Master Thesis Report (2021–2022)

Superconducting topological metamaterial coupled to flux-tunable transmon qubit:
toward analog quantum simulation with giant atoms



Abstract

This report presents the detailed description regarding the realization of a photonic multimode environment coupled to a flux-tunable artificial atom. This represents a step toward the realization of an analog quantum simulator, allowing for the experimental study of interacting two-level systems in structured environments. The platform consists of a metamaterial made out of an array of coupled Niobium Nitride (NbN) lumped-element microwave superconducting resonators, capacitively coupled to a magnetic flux-tunable transmon qubit. Thin NbN films allow to achieve extremely high kinetic inductance up to $90\text{pH}/\square$ due to their intrinsic disorder; on one side the resulting high impedance allows to achieve ultra-strong coupling regime, on the other it allows to realize extremely compact resonator arrays; Furthermore, such platform represents an extremely versatile device, allowing for the analog quantum simulation of a two-level system interacting with an engineered non-trivial photonic dispersion relation, such as SSH states exhibiting topological properties. The achievement of falling group velocity at the band edge of the photonic environment, allows for the study of atom-photon bound state; from the physical perspective, this represents a fundamental step toward the study of spin systems[24], device side instead, such platform's features allow for the realization of quantum random access memory for the future realization of large-scale, long-distance interacting qubit-based, quantum processors[17][12]. Engineering the metamaterial coupling allows for the exhibition of left-handedness, fundamental for the realization of high-kinetic inductance quantum-limited travelling wave parametric amplifiers (K-TWPA). In the context of this thesis, the system has been modeled, designed, numerically and FEM simulated, fabricated and experimentally characterized in a cryogenic environment.

A thesis presented for the international master degree in
Nanotechnologies for integrated circuits

by

Sbroggio' Davide

Supervisor: Gonnelli Renato
Instructor: Scarlino Pasquale
Tutor : Vincent Jouanny
Project Duration: 02,2022 - 08,2022
Group: Hybrid quantum circuit laboratory, EPFL

EPFL



Summary

This report aims to investigate the coupling between a multimode bosonic environment and an artificial atom-like two-level system.

In the following the main modeling, simulation, fabrication and measurement process will be explained in detail.

In chapter 1 an introduction to the topic will be given; the reasons behind the need of such a device are presented with a brief historical overview.

In chapter 2 the main theoretical basis, needed to understand the rest of the work, will be provided; fundamental cQED elements will be presented as Josephson Junctions, SQUID junctions and coplanar waveguide resonator working principle will be explain in details. Finally, a brief overview of electromagnetic field quantization will be given and the fundamental modeling of a simple qubit will be presented.

Chapter 3 will mostly deals with the modeling of the interaction between two-level systems and multimode cavity arrays; which is the main topic of this thesis.

In chapter 4 the design strategy will be presented, for each of the device's components; finally, simulations will be described prior to the fabrication process described in detail in chapter 5.

In chapter 6 the cryostat setup and cabling will be covered, together with the used measurement tools.

In chapter 7 experimental results are presented; the transmon qubit has been successfully made interact with the multimode bosonic system. Chapter 8 conclude this report and open future perspective on the system.

Contents

Summary	i
1 Introduction	1
2 Fundamentals concepts of superconductivity and cQED	2
2.1 Basic Concepts	2
2.2 Josephson Junctions	4
2.3 SQUID junctions	5
2.4 Superconducting resonators	6
2.4.1 Distributed resonators	6
2.4.2 Lumped resonators	8
2.5 Modelling of a single cavity	9
2.6 Modelling of a qubit	10
2.6.1 Transmon qubit	11
3 Coupling two-level systems to multimode environment	12
3.1 Coupled cavity arrays	12
3.1.1 Resonator - Resonator interaction	12
3.1.2 Generalization to N-resonator coupling and different regimes	13
3.1.3 Qubit - Single Cavity interaction: Jaynes-Cummings model	17
3.2 Qubit coupled to single and multimode system	20
3.2.1 Transmon qubit coupled to single resonator in a metamaterial	20
3.2.2 Atom-photon bound state	21
3.2.3 Transmon qubit coupled to multiple resonators in a metamaterial	22
4 A device to achieve analog quantum simulation	25
4.1 Design approach	25
4.1.1 General Overview	25
4.1.2 Superconducting multi-mode metamaterial	25
4.1.3 Transmon qubit	28
4.1.4 Read-out resonator	29
4.1.5 Flux Line	30
4.1.6 Quantum State control feed line	30
4.1.7 Final Design	31
4.2 Validating the design by means of structural and behavioral simulations	32
4.2.1 Electrostatic simulations: capacitance distribution	32
4.2.2 Dynamic simulations: Behavioural analysis	33
5 Device fabrication - Process Flow in details and alternatives solutions	34
5.1 The need of a platform - Investigating possible alternative	34
5.2 Platform fabrication processes - Detailed Description	35
6 Measurement set-up	44
6.1 Dry dilution cryostat	44
6.2 Room temperature set-up	45
6.2.1 IQ mixing	45

7	Experimental results	47
7.1	Time of Flight	47
7.2	Read out resonator characterization	48
7.3	Punch out	49
7.4	Multi-mode environment	50
7.5	Transmon coupled to metamaterial	51
7.6	Two tones spectroscopy	52
8	Conclusion	53
	References	54

1

Introduction

On May 1981, Richard Feynman published an article [7] where he question himself with the following: "Can a quantum system be probabilistically simulated by a classical (probabilistic, I'd assume) universal computer?. [...]The answer is certainly, No! [...] and this arise from the hidden-variable problem which implies that it is impossible to represent the results of quantum mechanics with a classical universal device."

In other words, Feynman stated that to properly simulate the behaviour of a quantum system, the computer itself has to be build of quantum mechanical elements which obey quantum mechanical laws. Since then, many progresses have been achieved in the field [2, 15].

This thesis represents a step toward analog quantum simulations, where the interaction between a two level system and a bosonic bath are simulated by means of quantum hardware, i.e, hardware which inherently obeys quantum mechanical laws[11]. In other words, it's of particular interest to study the interaction between an "impurity" (small system with few degrees of freedom) and an "environment" or "bath" (large system with numerous degrees of freedom). [23]

Regarding this, spin boson models can be used to simulate dissipation in quantum mechanics and to study light-atom interaction. To model dissipation, a two level system is coupled to a bath of bosonic modes described by harmonic oscillators.

In the interaction between a single two level system and a bosonic environment, three coupling regimes can be defined:

- Individual mode coupling: The qubit is coupled with single resonator mode.
- Multimode coupling: The qubit is coupled to several modes of the system; this occurs for a coupling strength g larger than the free spectral range $\Delta\omega$; where the free spectral range is defined as the frequency difference between to modes of multimode system.
- Ultrastrong multimode coupling: when the coupling strength g become comparable to the qubit transition frequency ω_q and the condition $g > \Delta\omega$ is maintained, the qubit ultra strongly couples to several modes, breaking down rotating wave approximation and leading the number of excitation in the system to be no longer conserved in absence of external drive. This working regime has to be reached in order to realize spin-boson model; in order to do so, high impedance resonators have to be use.

It is on the scope of this thesis to realize a device that points toward the future development of giant atoms systems ultra-strongly coupled to a multimode system. In quantum optics it is common to assume that atoms can be approximated as point-like compared to the wavelength of the light they interact with. However, recent advances in superconducting circuit demonstrate the feasibility in realizing artificial atoms coupled to an electromagnetic field in multiple points, spaced wavelength apart.[8]

Multiple coupling points give rise to interference effects, such as decoherence-free interaction and frequency dependent giant atom coupling to the environment.[9]

2

Fundamentals concepts of superconductivity and cQED

2.1. Basic Concepts

In 1911 has been observed that a certain type of materials exhibit perfect conductivity when exposed to cryogenic environment. In particular Onnes showed absence of electrical resistivity in Mercury. In 1933 Ochsensfeld and Meissner they first experimentally prof that when superconductor are cooled down below their critical temperature, the magnetic field is expelled from the material's bulk, resulting in perfect diamagnetism. In 1914, Onnes showed the existence of a critical magnetic field that set the boundary above which a superconducting material stop exhibit superconducting properties. In 1913, Onnes discovered the existence of a critical current; consequence of the critical field, able to break superconducting properties;

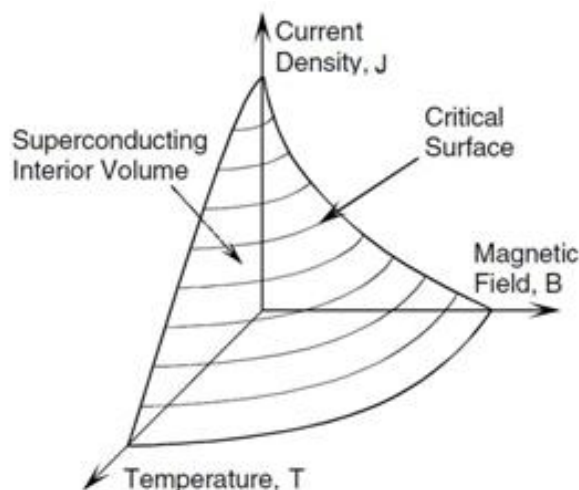


Figure 2.1: Critical surface representation; above the critical field parameters, the material stop exhibiting superconducting properties.

Magnetic properties of the material allow to distinguish among type 1 and type 2 superconductors; in particular in type 1 superconductors, the critical field experimentally observed, coincide with the thermodynamic critical field. Generally type 1 superconductor has lower critical temperature than type 2. Among the superconductors used in this thesis it's relevant to highlight that Aluminum has a critical temperature (T_c) of 1.18 K, while Niobium Nitride (NbN), type 2 superconductor, has a critical temperature of 16 K.

The first set of equation aiming to analytically describe the phenomena, takes their names from the German physicist Fritz London; he proposed to subdivide the overall current in a superconducting material in a dissipation less component and a quasi particle dissipative one.

$$d\vec{J}_s/dt = n_s e^2 / m \vec{E} = \vec{E} / \lambda \quad (2.1)$$

where J_s is the dissipation-less current, n_s is the fraction of superconducting electrons, m is the electron mass, and λ is the London penetration depth. The second London equation reads as follow:

$$\nabla \times \lambda \vec{J}_s = -\vec{B} \quad (2.2)$$

In 1957, more than 55 years after superconductivity first evidence, Bardeen, Cooper and Schrieffer discovered the microscopic origin of the phenomenon, proposing the well known BCS theory. Such a theory, is based on the existence of attractive interaction among electrons mediated by phonons, which leads to the formation of Cooper pairs.

According to the theory, the interaction phonon-electrons, under certain conditions become attractive resulting in Fermi sea instability leading to the formation of a new superconducting ground state, made by a certain number of electrons paired in Cooper pairs, with overall energy inferior to the one of those taken independently.

2.2. Josephson Junctions

A Josephson junction is formed by separating two superconducting electrodes with an insulating thin layer, such to allow for the quantum mechanical tunnelling through it.

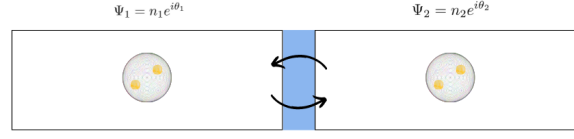


Figure 2.2: Schematic representation of Josephson tunnel junction; two superconducting electrodes are separated by mean of a thin oxide layer such to allow for the tunneling of Cooper pairs between left and right superconducting layers.

Due to the superconducting states, cooper pairs in the superconducting material can be described by the following complex order parameter $\Psi_{1,2} = \sqrt{n_{1,2}}e^{i\theta_{1,2}}$, where $n_{1,2}$ indicate the number of Cooper pairs and $\theta_{1,2}$ the superconducting phase in each superconducting layer. The electrical behaviour of a Josephson junction is explained in term of the Josephson effect; the I-V characteristic can be express as follow:

$$I_J = I_o \sin(\delta), \quad (2.3)$$

$$V = \Phi_o \delta / 2\pi, \quad (2.4)$$

where δ indicated the difference between the two superconducting phases: $\theta_2 - \theta_1$, I_0 is the critical current above which the JJ become dissipative, $\Phi_o = h/2e$ is the magnetic flux quantum and V is the voltage across the junction. [16]

By differentiating the Josephson equation for the current the following relation is obtained:

$$\frac{dI_J}{dt} = I_o \cos \delta \frac{2\pi}{\Phi_o} V \quad (2.5)$$

which is the equation of an inductor with inductance:

$$L_J = \frac{\Phi_o}{2\pi I_o \cos \delta} \quad (2.6)$$

Explicitly writing the dependence on the critical current, the inductance expression can be written as follow:

$$L = L_{J_0} / \sqrt{1 - (I/I_0)^2} \quad (2.7)$$

A fundamental property is then showed: a Josephson junction behave as a dissipation-less non linear inductor; as will be clear in the following chapters, this feature will be key in the realization of artificial atoms. The energy stored in the junction can be easily calculated as the time integral of the product between the voltage and the current across the junction, resulting in:

$$U_J = E_J [1 - \cos \delta] \quad (2.8)$$

where $E_J = \Phi_o I_0 / 2\pi = \hbar I_0 / 2e$ is called Josephson energy.

2.3. SQUID junctions

A DC SQUID (Superconducting QUantum Interference Device) is a device consisting of two Josephson junctions connected in parallel to form a closed superconducting loop.

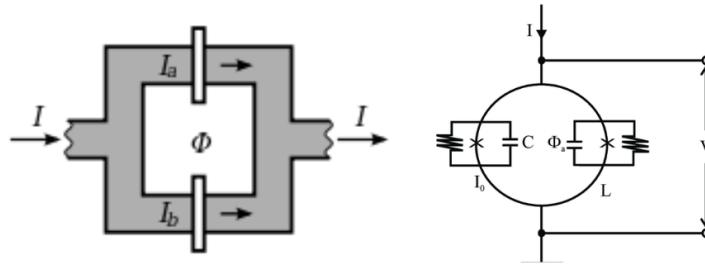


Figure 2.3: Schematic of a DC SQUID junction; two Josephson junctions are closed in a loop forming a magnetic flux quanta sensitive device. The right figure[5] shows an equivalent circuit that takes into account for the quasi particle tunneling

The total current through the parallel junction is:

$$I = I_a + I_b = I_{c1}\sin\delta_1 + I_{c2}\sin\delta_2 \quad (2.9)$$

and taking into account of the relationship between δ_1 and $\delta_2 \rightarrow \delta_2 = \delta_1 - 2\pi\Phi/\Phi_0$ [4] the total current then become:

$$I = I_a + I_b = I_{c1}\sin\delta_1 + I_{c2}\sin(\delta_1 - 2\pi\Phi/\Phi_0) \quad (2.10)$$

By supposing the the critical currents of the two junctions equals, the critical current dependence on the external applied magnetic flux is written as follow:

$$I_0^{SQUID} = 2I_0|\cos(\pi\Phi_{ext}/\Phi_0)| \quad (2.11)$$

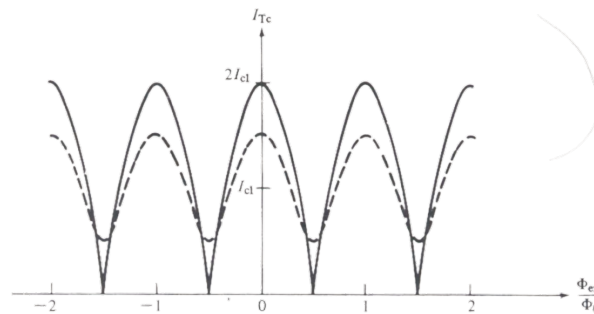


Figure 2.4: Dependence of the critical current on the externally applied magnetic flux; solid line for symmetrical junctions with $I_{c1} = I_{c2}$, broken line for symmetrical junctions with $I_{c1} = 2I_{c2}$ [4]

Fig. 2.4 shows the critical current trend versus the externally applied magnetic flux. The SQUID junction will be integrated into the transmon design as a dissipation-less non linear flux tunable inductance, resulting in an artificial atom with flux tunable resonance frequency.

2.4. Superconducting resonators

Superconducting resonators are one of the key elements in circuit QED; they are particularly useful for a variety of applications ranging from single photon detection, parametric amplification, narrow band filtering and quantum information processing [25]. Resonators can be divided into distributed and lumped basing on their dimensions with the respect to the operating electromagnetic wavelength. In the following the main equation describing resonators will briefly presented to help in the overall report understanding.

2.4.1. Distributed resonators

If the physical dimension is comparable to the operating wavelength, resonators are said to be distributed. In opposition to lumped resonators, the signal travelling trough them vary along the line and between elements; this results in signal experiencing a non negligible phase change across various points.[25]

Coplanar waveguide transmission line

The coplanar waveguide (CPW) is a distributed resonant circuit, made out of a central conductor of width, w , spaced by a distance, d , from the surrounding ground plane. The characteristic impedance of a transmission line is given by:

$$Z = \sqrt{L_d/C_d} \quad (2.12)$$

where L_d and C_d are the inductance and capacitance per unit length. In order to be efficiently interface with standard hardware, CPW transmission line are usually designed to have a characteristic impedance of 50 Ohm, minimizing signal reflection. [25] The inductance can be expressed as $L = L_g + L_k$ with L_g being the geometric inductance and L_k the kinetic inductance. Geometric inductance and capacitance can be expressed as follow:

$$L_g = \mu_0 K(k')/4K(k) \quad (2.13)$$

$$C = 4\mu_0\epsilon_{eff}K(k)K(k') \quad (2.14)$$

where μ_0 and ϵ_0 are the vacuum permeability and permittivity, K is the elliptic integral of the first kind, $k = w/(w+2d)$ and $k' = \sqrt{1-k^2}$, with w the center conductor width and d the gap width to the ground plane.

Coplanar waveguide resonators

CPW resonator can be made out of CPW transmission line by simply introducing impedance mismatch at the extremity of the CPW length. An open end boundary condition imposes a voltage anti-node, whereas a shorted end imposes a voltage node.[25]

A resonators with two open ends has a fundamental mode of wavelength $\lambda/2$ with resonance frequency:

$$\omega_r = 2\pi/2l\sqrt{L_dC_d} \quad (2.15)$$



Figure 2.5: Realistic representation of a coplanar waveguide resonator; the signal travel along the central conductors of width w , spaced from the ground plane by a trench of width d . On the bottom the equivalent circuit representation is shown; the CPW is modeled as an LC distributed transmission line

being l the overall CPW length. If the CPW transmission line is instead open on one side and grounded on the other, it creates a resonator with fundamental mode of wavelength $\lambda/4$ and resonance frequency $\omega_r/2$

Transmission style resonator When the CPW transmission line is interrupted at the two extremity, separated by a distance l , the two gaps act as mirrors in cavity QED.[25] The electrical behaviour can be described in term of complex $S_{i,j}$ parameters; for an example S_{21} parameter represent the ratio between the voltage wave at the output 2 versus the input voltage at the input 1. In such configuration the only signal that will be transmitted is the one that match the resonance frequency ω_r of the resonator. In term of power transmitted signal, $|S_{21}|^2$, the system will exhibit a peak in correspondence of the resonator frequency and a phase shift around ω_r . The resonance profile in the power spectrum follows a Lorentzian line-shape:

$$F_T(\omega) = A \frac{\kappa}{(\omega - \omega_r)^2 + (\kappa/2)^2} \quad (2.16)$$

where κ is a fundamental parameter that represent the photon decay rate and it correspond the full width at half maximum (FWHM); such parameters is express as the ratio between the energy stored in the resonator and the power loss. The photon decay rate allow to compute the quality factor of the resonator:

$$Q = \omega_r / \kappa \quad (2.17)$$

The resonator loses part of his energy coupling through different losses channel, as the transmission line, and through the electrically and magnetically coupling to its surrounding. The total cavity decay rate is than decomposed into:

$$\kappa = \kappa_{ext} + \kappa_{int} \quad (2.18)$$

where κ_{ext} takes into account for the decay due to coupling with the transmission line through an overall capacitance C_{ext} Any additional loss is instead Incorporated in the κ_{int} term. The total quality factor is also decomposed in the same way as:

$$1/Q = 1/Q_{ext} + 1/Q_{int} \quad (2.19)$$

The major channel losses that contribute to κ_{int} are due to: resistive losses (Q_{res}), Dielectric losses (Q_{diel}) and microwave leakage (Q_{leak}).[25] All these terms simply sum up, defining the total internal quality factor as:

$$1/Q_{int} = 1/Q_{res} + 1/Q_{diel} + 1/Q_{leak} \quad (2.20)$$

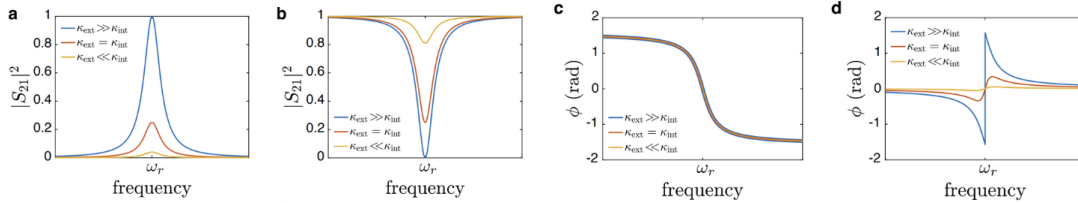


Figure 2.6: Figure a,c shows respectively the power spectrum and the phase for a CPW resonator in transmission style. Analogously figure b,d show the power spectrum and the phase for a CPW resonator in hanged configuration; different coupling regimes are shown[25]

This allow to identify three resonators coupling regimes:

- $k_{ext}/k_{int} > 1 \rightarrow$ over-coupled
- $k_{ext}/k_{int} = 1 \rightarrow$ critically coupled
- $k_{ext}/k_{int} < 1 \rightarrow$ under-coupled

The choice to works in an particular region mostly depend on the target application; for readout its particular convenient to work in over-coupled regime, allowing for photon "release" in the read out waveguide. For quantum bus and quantum memory application, its preferable to work in under-coupled regime such to maximise the photon lifetime.

Hanged style resonator In this case the CPW resonator is placed adjacent to transmission line called feed line, capacitively or inductively coupled to it. The transmitted power spectrum shows a dip when the propagating signal match the resonance frequency of the hanged resonator. This phenomena can be seen as a destructive interference between the photon in the waveguide and the photon exiting the resonator shifted in phase.

2.4.2. Lumped resonators

If the size of an element is smaller than the wavelength of the applied signal, the resonator is said to be lumped; in such situation the effect of the wave propagation can be neglected; being so the phase difference between input and output is minimal.[25] With respect to the inductance (L_d) and capacitance (C_d) of the distributed resonator, those for the lumped resonator are: $C_{lum} = C_d l/2$ and $L_{lum} = 2L_d l/n^2 \pi^2$; the impedance of the lumped element resonator relates to the distributed element impedance as:

$$Z_n = 2Z_r/n\pi \quad (2.21)$$

High-impedance resonators

Fundamental importance in this thesis has been given to the study and realization of High Impedance resonators. By increasing the resonator impedance much over the standard 50 Ohm it is possible to enhance zero-point fluctuations of voltage, optimizing the resonator for electric dipole coupling to two-level systems.[25] A common and extremely efficient method in cQED to increase the resonators impedance is through the usage of the high kinetic inductance of strongly disordered superconducting material such as NbN. The kinetic inductance is expressed in terms of microscopical quantities as:

$$L_k = \frac{m_e l}{2n_s e^2 w d} \quad (2.22)$$

or design level conveniently in term of geometrical quantity and kinetic inductance per square as:

$$L_k = L_{\square} l/w \quad (2.23)$$

These resonators are particularly suited for coupling to systems with relatively small electric dipole moments; the capacitive coupling indeed is $\propto \sqrt{Z}$

2.5. Modelling of a single cavity

The electromagnetic field will be first classically described by Maxwell equations; it will be then discretized following the conventional quantization described in quantum optics literature. Following [16]; let's first describe an electromagnetic field spatially confined in a one-dimensional cavity. Considering two infinite superconducting walls separated by a distance L .

Assuming the electric field has polarization along x , and assuming the cavity is free of any external current or charge, Maxwell equations can be stated as follow:

$$\nabla \times \vec{E} = -\partial \vec{B} / \partial t \rightarrow \partial E_x(z, t) / \partial z = -\partial B_y(z, t) / \partial t \quad (2.24)$$

$$\nabla \times \vec{B} = \epsilon_0 \mu_0 \partial \vec{E} / \partial t \rightarrow -\partial B_y(z, t) / \partial z = \epsilon_0 \mu_0 \partial E_x(z, t) / \partial t \quad (2.25)$$

$$\nabla \cdot \vec{E} = 0 \rightarrow \partial E_x(z, t) / \partial x = 0 \quad (2.26)$$

$$\nabla \cdot \vec{B} = 0 \rightarrow \partial B_y(z, t) / \partial y = 0 \quad (2.27)$$

Given perfect conducting walls. the electric field must vanish at the boundaries, $E_x(z = 0, t) = 0$ and $E_x(z = L, t) = 0$. This result in the following solution:

$$E_x(z, t) = \mathcal{E} q(t) \sin(kz) \quad (2.28)$$

$$B_y(z, t) = \mathcal{E} \frac{\mu_0 \epsilon_0}{k} \dot{q}(t) \cos(kz) \quad (2.29)$$

where $\mathcal{E} = \sqrt{\frac{2\omega_c^2}{V\epsilon_0}}$ with V the effective volume of the cavity and $k = m\pi/L$, $m = 1, 2, \dots$ is the wave number corresponding to the frequency $\omega_c = k/\sqrt{\mu_0\epsilon_0}$;

$q(t)$ describe the time evolution of the system and has the dimension of a length, each integer m correspond to one mode of the cavity. The cavity has discrete mode, nonetheless each mode can have continuous amount of energy. The energy of the **single mode** can indeed be written as:

$$H = \frac{1}{V} \int dV \left(\frac{\epsilon_0}{2} |E_x(z, t)|^2 + \frac{1}{2\mu_0} |B_y(z, t)|^2 \right) \quad (2.30)$$

which taking into account of the analytical form of \vec{E} and \vec{B} it become:

$$H = \frac{1}{2} [p^2(t) + \omega_c^2 q^2(t)] \quad (2.31)$$

which is the energy of a classical harmonic oscillator if considering $q(t)$ and $p(t) = \dot{q}(t)$ as the canonical position and momentum. The Hamiltonian can be treated quantum mechanically by promoting the canonical parameters to be quantum operators. This result in a quantum Hamiltonian for the harmonic oscillator:

$$\hat{H} = \frac{1}{2} [\hat{p}(t)^2 + \omega_c^2 \hat{q}(t)^2] \quad (2.32)$$

therefore **each mode of the cavity act as a quantum harmonic oscillator**; defining the non-Hermitian operators:

$$\hat{a} = (\omega_c \hat{q} + i\hat{p}) / \sqrt{2\omega_c} \quad (2.33)$$

$$\hat{a}^\dagger = (\omega_c \hat{q} - i\hat{p}) / \sqrt{2\omega_c} \quad (2.34)$$

The electric and magnetic fields can now be written as:

$$\hat{E}_x(z, t) = \mathcal{E}_0 (\hat{a} + \hat{a}^\dagger) \sin(kz) \quad (2.35)$$

$$\hat{B}_y(z, t) = i\mathcal{B}_0 (\hat{a} - \hat{a}^\dagger) \cos(kz) \quad (2.36)$$

and the Hamiltonian for the single mode can be re-written as:

$$\hat{H} = \omega_c (\hat{a}^\dagger \hat{a} + 1/2) = \omega_c (\hat{n} + 1/2) \quad (2.37)$$

where $\hat{n} = \hat{a}^\dagger \hat{a}$ is the number operator. The Hamiltonian of the system is then:

$$\hat{H} |n\rangle = E_n |n\rangle \quad (2.38)$$

where $|n\rangle$ are the Fock states representing the energy eigenstates for the single mode cavity, with corresponding energy $E_n = \omega_c(n + 1/2)$. The quantum state of the cavity is in general a linear combination of Fock states in the form $\sum_n c_n |n\rangle$

2.6. Modelling of a qubit

The main idea behind the realization of a qubit, is to realize a system where ground and excited states can be properly identified. To do so, a non-linear (anharmonic) oscillator must be obtain; such non linearity can be easily obtained out of a Josephson junction, using only the two lowest energy states as a qubit.

The transmon circuit consist of a JJ shunted by a relatively large capacitor, as depicted in figure:

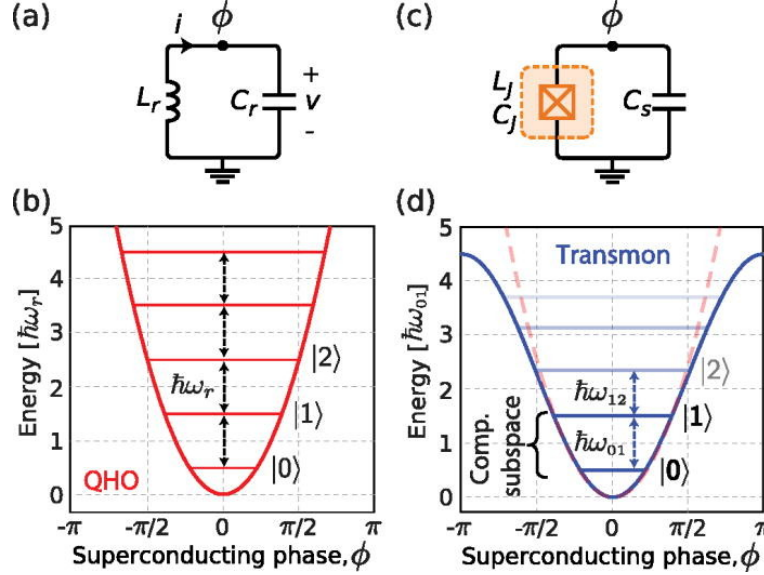


Figure 2.7: Figure [a] shows the equivalent LC circuit of an harmonic oscillator; figure [b] shows the resulting potential and eigenvalues distribution. Figure [c] shows the equivalent circuit for an anharmonic quantum oscillator; the non linearity is given by the presence of the Josephson junction acting as a non linear inductance. Figure [d] shows the potential energy distribution for the anaharmonic oscillator with its new eigenvalues. [14]

the total energy of the transmon results to be:

$$H_{trans} = Q^2/2C + E_J[1 - \cos(\delta)] \quad (2.39)$$

and writing the total charge Q in terms of number of cooper pair, the energy becomes:

$$\hat{H}_{trans} = 4E_c\hat{m}^2 + E_J[1 - \cos\hat{\delta}] \quad (2.40)$$

Being \hat{m} and $\hat{\delta}$ are the operator referring to the canonical momentum and position.

In order to find the energy transition of the transmon, the eigenvalues and eigenvector of this Hamiltonian must be found:

in the limit of $E_J/E_C \gg 1$, the second term can be expanded, obtaining the harmonic oscillator Hamiltonian, plus a non linear term:

$$\hat{H}_{trans} = 4E_c\hat{m}^2 + E_J\delta^2/2 - E_J\delta^4/24 + \dots \quad (2.41)$$

the first two terms are analogous to an harmonic LC circuit, such that

$$\omega_j = \sqrt{8E_JE_c} \rightarrow \omega_{LC} = 1/\sqrt{LC} \quad (2.42)$$

Rewriting than the Hamiltonian in term of b and b^\dagger , it becomes:

$$\hat{H}_{trans} = \omega_{01}\hat{b}^\dagger\hat{b} + \alpha/2\hat{b}^\dagger\hat{b}^\dagger\hat{b}\hat{b} \quad (2.43)$$

where we arrived at an Hamiltonian for an anharmonic oscillator with a lower energy transition: $\omega_{01} = \sqrt{8E_JE_c} - E_c$ and anharmonicity $\alpha/2\pi = -E_c$.

Therefore the transmon circuit behave as a two level system which can be described as a pseudo spin with the Pauli operator:

$$\hat{H}_q = -\frac{\omega_q}{2}\sigma_z \quad (2.44)$$

where ω_q is the lowest transition in the transmon circuit.

2.6.1. Transmon qubit

A transmon qubit is the name conventionally given to an artificial two level system with certain characteristic. As shown in the previous section, the Hamiltonian of an artificial atom is the one of an anharmonic oscillator, with a given kinetic and potential energies equivalents. In particular, recalling equation 2.39, the kinetic energy is the energy stored in the capacitor, which quadratically scale with the charge, and the potential energy is the non linear inductive term due to the magnetic field stored in the non linear inductor. A first important thing to notice is that the Hamiltonian may be dominated by the term E_C or E_J resulting in a qubit in different working regimes.

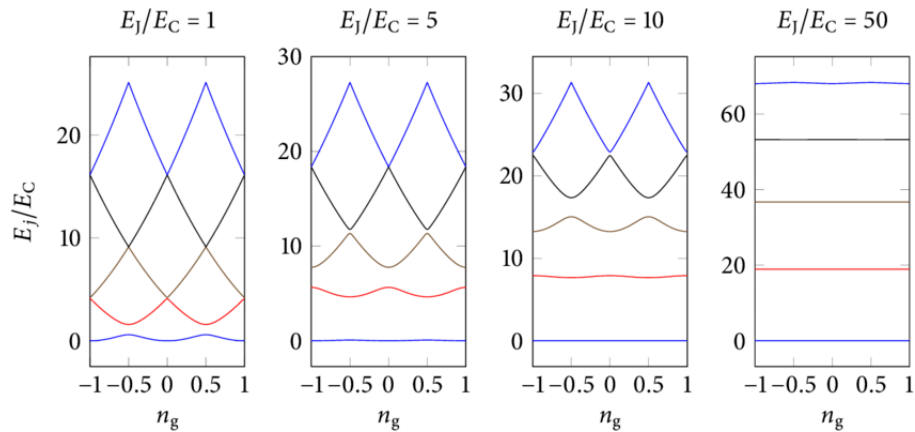


Figure 2.8: Different eigenvalues distribution are shown highlighting the possible working regimes of an artificial two level system. On the extreme left it can be seen that on Cooper pair regime, noise in the system may induce unwanted excitation; on the contrary, top right figure shows the eigenvalues for a qubit in transmon regime; the system is much more robust against noise.[19]

If the term $E_J \gg E_C$ the system become extremely sensitive to flux noise, on the other side, if $E_C \gg E_J$ the system is sensible to charge noise. Nonetheless, it has been demonstrated that is experimentally much easier and efficient to control the charge noise, hence the community used to work in a regime where $E_J \approx 40E_C$ the so called transmon regime. From the 2.8 it can be seen how in such configuration, the energy level are equally spaced.

3

Coupling two-level systems to multimode environment

3.1. Coupled cavity arrays

In the following a simple description of the light-matter interaction where a two level quantum system (qubit) interacts only with a single mode of light [16] will be carried out.

3.1.1. Resonator - Resonator interaction

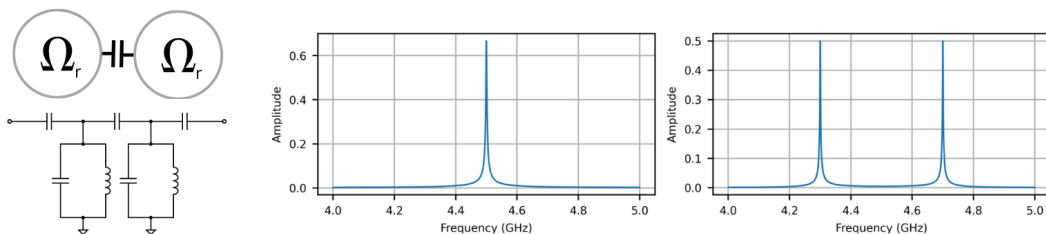


Figure 3.1: On the left, the equivalent circuit of coupled harmonic resonator; on the right, the transmission spectrum $|S_{21}|^2$ for the single and coupled cavities is shown.

As seen in the previous section, the Hamiltonian for a single cavity or resonator, corresponds to the one of the simplest quantum harmonic oscillator; it can indeed be written in terms of creation and annihilation operators as follow:

$$\hat{H}_{res} = \omega_r \left(\hat{a}^\dagger \hat{a} + \frac{1}{2} \right) \quad (3.1)$$

Let's now considered two resonators coupled together by means of a coupling strength g ; The Hamiltonian for the two separate resonators is written as:

$$\hat{H}_{ri} = \omega_{ri} \left(\hat{a}_i^\dagger \hat{a}_i + \frac{1}{2} \right) \quad i = 1, 2 \quad (3.2)$$

the coupling Hamiltonian read instead as follow:

$$\hat{H}_{r1,r2} = g_{r1,r2} (\hat{a}_1^\dagger \hat{a}_2 + \hat{a}_2 \hat{a}_1^\dagger + \hat{a}_1^\dagger \hat{a}_2^\dagger + \hat{a}_1 \hat{a}_2) \quad (3.3)$$

with g being the coupling strength; the two terms: $\hat{a}_1\hat{a}_2$ and $\hat{a}_1^\dagger\hat{a}_2^\dagger$ are less likely to occur, they can be than average out by the so called "Rotating Wave approximation" (RWA). The final Hamiltonian of the two coupled system read than as follow:

$$\hat{H}_{r,r} = \omega_{r1}(\hat{a}_1^\dagger\hat{a}_1 + \frac{1}{2}) + \omega_{r2}(\hat{a}_2^\dagger\hat{a}_2 + \frac{1}{2}) + g_{r1,r2}(\hat{a}_1^\dagger\hat{a}_2 + \hat{a}_2\hat{a}_1^\dagger) \quad (3.4)$$

the Hamiltonian can be conveniently written down in its matrix formulation as follow:

$$H_{r,r} = \begin{pmatrix} \omega_{r1} & g_{r1,r2} \\ g_{r1,r2} & \omega_{r2} \end{pmatrix}$$

which diagonalization leads to the following set of eigenvalues:

$$\omega_{\pm} = (\omega_{r1} + \omega_{r2})/2 \pm \sqrt{(\omega_{r1} - \omega_{r2})^2 + 4g^2}/2 \quad (3.5)$$

3.1.2. Generalization to N-resonator coupling and different regimes

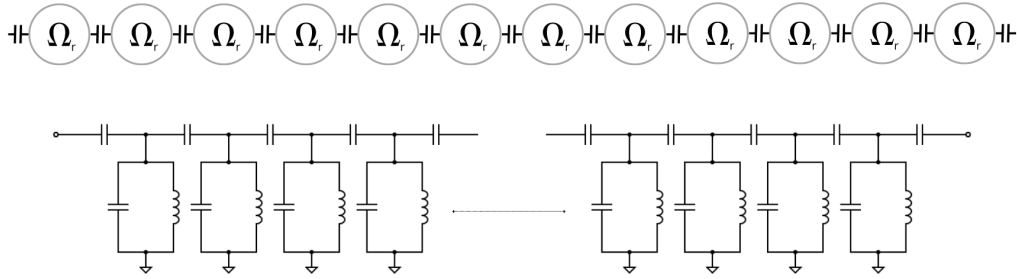


Figure 3.2: Equivalent circuit of a metamaterial made out of coupled cavities array. The figures shows the equivalent circuit model as a series of lumped LC resonators.

To show the multi-modal behaviour of the metamaterial, the last formulation can be generalized to N resonators coupled together. The Hamiltonian of the resulting meta-material can be easily expressed as follow:

$$\hat{H}_{mm} = \sum_i \omega_{R_i}(\hat{a}_i^\dagger\hat{a}_i + \frac{1}{2}) + \sum_{j,i} g_{r_i,r_j}(\hat{a}_i^\dagger\hat{a}_j + \hat{a}_j\hat{a}_i^\dagger) \quad (3.6)$$

where rotating wave approximation has been already conveniently applied.

The matrix formulation for such Hamiltonian can be than written as:

$$\hat{H}_{m,m} = \begin{pmatrix} \omega_{r1} & g_{r1,r2} & \cdots & g_{r1,rn} \\ g_{r1,r2} & \omega_{r2} & \cdots & g_{r2,rn} \\ \vdots & \vdots & \ddots & \vdots \\ g_{rn,r1} & g_{rn,r2} & \cdots & \omega_{rn} \end{pmatrix}$$

As said before, to each single mode of the system, is associated a quantum harmonic oscillator, hence for a system of N coupled resonators, N eigenstates are possible, each of those representing a certain potential spatial photonic distribution.

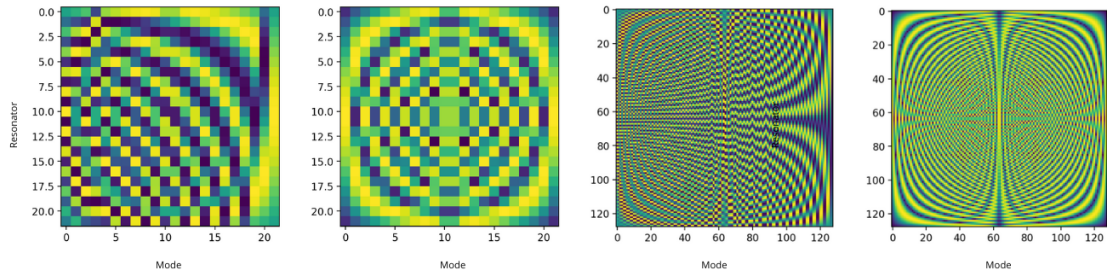


Figure 3.3: Numerical simulation of the eigenstate for the coupled cavities array. Horizontally is shown each of the system mode, vertically the resonator location in the metamaterial (space distribution). starting from the left, simulation of 22 resonators array, absolute values and raw data; on the right, simulation performed for 128 resonators, absolute value and raw data.

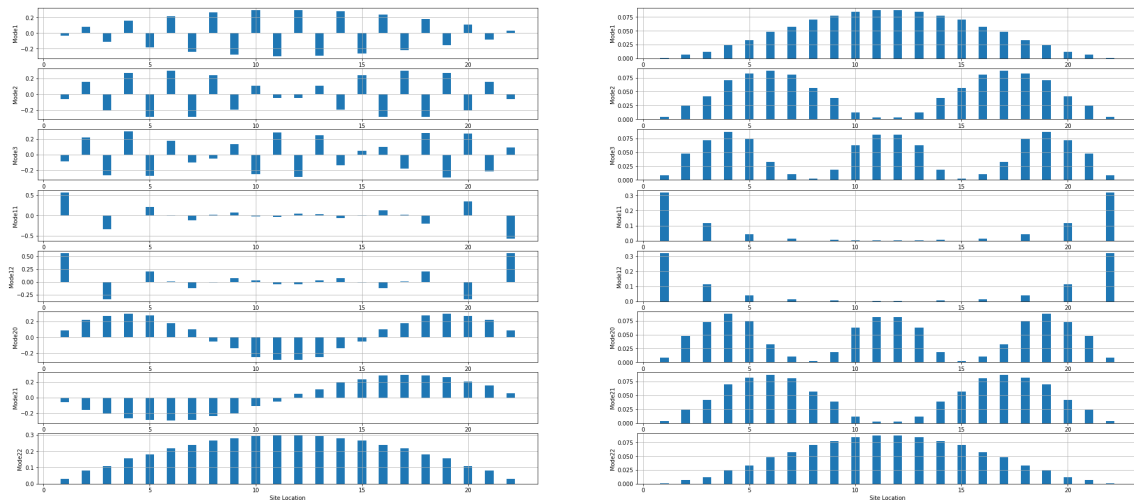


Figure 3.4: Numerical simulation of the eigenstate for the coupled cavities array. Horizontally is shown each of the system mode, vertically the resonator location in the metamaterial (space distribution). starting from the left, simulation of 22 resonators array, absolute values and raw data; on the right, simulation performed for 128 resonators, absolute value and raw data.

SSH Model

Let's now consider a system with N resonators coupled in a dimerized fashion as shown in the following figure:

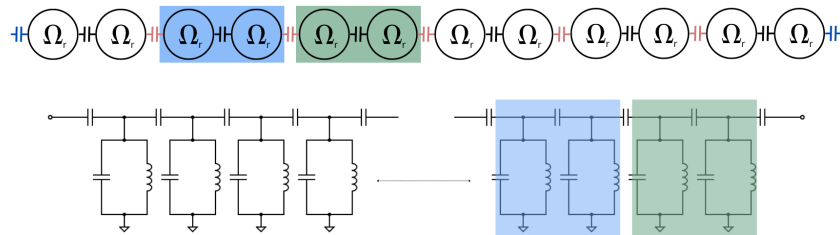


Figure 3.5: Schematic and equivalent circuit of a dimerized metamaterial; the resonators are coupled two by two

Each unit cell has a size L and has two sites A and B . Su, Schrieffer and Heeger published a theoretical study on polyacetylene in 1979, which focused on describing electrons hopping along this one-dimensional chain with alternating hopping amplitudes[21]; this model is called SSH model. In the following such model is applied, allowing to analytically show the importance of the structure. The staggered hopping amplitudes are denoted as t for intra-cell

hopping and γt for inter-cell hopping. The state of the chain is described by $|n, S\rangle$ with n the index of the unit cell $n \in \{0, N\}$ and $S \in \{A, B\}$. In the n -th cell, two possible intracell processes are possible:

$$|n, A\rangle \rightarrow t |n, B\rangle \quad (3.7)$$

$$|n, B\rangle \rightarrow t |n, A\rangle \quad (3.8)$$

Among the cell n and the cell $n+1$ the following process instead can occur:

$$|n, B\rangle \rightarrow |n+1, B\rangle \quad (3.9)$$

$$|n+1, A\rangle \rightarrow t |n, B\rangle \quad (3.10)$$

The Hamiltonian of the full system is simply given by summing up over all the cells n :

$$\hat{H}_{ssh} = t \sum_{n=1}^N (|n, B\rangle \langle n, A| + |N, A\rangle \langle n, B|) + \gamma t \sum_{n=1}^{N-1} (|n+1, A\rangle \langle n, B| + |N, B\rangle \langle n+1, A|) \quad (3.11)$$

The system can now be split into a bulk and boundary. The boundary corresponds to the external resonators, the bulk instead is made out of the central parts of the resonators array. Applying now Born-von Karman boundary condition on the central cavity array, the system can be thought as a chain closed in a loop, such that for N unit cells, the $(N+1)$ -th will be equivalent to the first one. The Hamiltonian can then be written as:

$$\hat{H}_{bulk} = \sum_{n=1}^N t (|n, B\rangle \langle n, A| + |N, A\rangle \langle n, B|) + \gamma t (|(n \bmod N) + 1, A\rangle \langle n, B| + |N, B\rangle \langle (n \bmod N) + 1, A|) \quad (3.12)$$

The eigenstate $|\Psi_l(k)\rangle$ of the Hamiltonian:

$$\hat{H}_{bulk} |\Psi_l(k)\rangle = E_l(k) |\Psi_l(k)\rangle \quad (3.13)$$

has to be determined. Due to translational invariance, Bloch theorem is applied searching for eigenstate in the form of plane waves. Introducing the plane wave basis states as:

$$|k\rangle = \frac{1}{\sqrt{N}} \sum_{m=1}^N e^{imk} |m\rangle \quad (3.14)$$

The eigenstate becomes:

$$|\Psi_n(k)\rangle = |k\rangle |u_n(k)\rangle, \quad \text{with } |u_n(k)\rangle = a_n(k) |A\rangle + b_n(k) |B\rangle \quad (3.15)$$

where $|u_n(k)\rangle$ belong to internal degree of freedom, and are eigenstate of the bulk momentum space Hamiltonian:

$$\hat{H}(k) |u_l(k)\rangle = E_l(k) |u_l(k)\rangle \quad (3.16)$$

with $\hat{H}(k)$ defined as:

$$\hat{H}(k) = \langle k | \hat{H}_{bulk} | k \rangle \quad (3.17)$$

or in matrix form:

$$\hat{H}(k) = \begin{pmatrix} 0 & t(1 + \gamma e^{-ik}) \\ t(1 + \gamma e^{ik}) & 0 \end{pmatrix}$$

with eigenvalues:

$$E_{\pm}(k) = \pm \sqrt{|t + \gamma t e^{-iLk}|^2} = \pm |t + \gamma t e^{-iLk}| = \pm t \sqrt{1 + \gamma^2 + 2\gamma \cos(Lk)} \quad (3.18)$$

Different regimes can now be identified for different γ values. For $\gamma = 0$ the chain is simply made out of isolated dimers, being the intercell hopping term $\gamma t = 0$. This configuration takes the name of fully dimerised chain. More interesting is the behaviour of the system for $\gamma \neq 0$

Normal Configuration For $\gamma = 1$ the intra- and inter- cell coupling are equals.

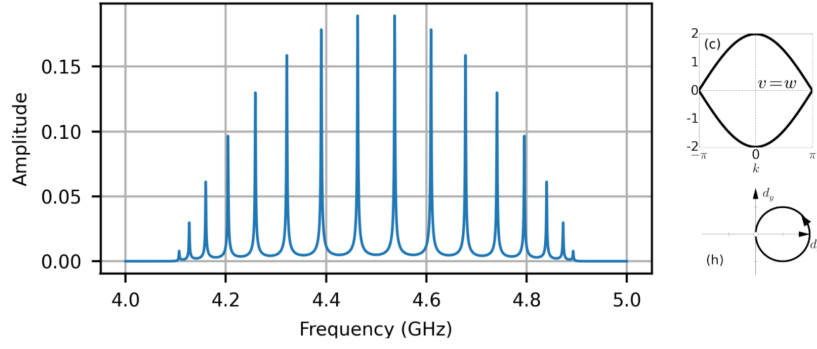


Figure 3.6: Normal configuration; on the left the transmitted power is shown [23]; on the right dispersion relations and representation in d_x, d_y plane [3]

Trivial Configuration For $0 < \gamma < 1$ the intracell coupling is bigger than the intercell coupling. The dispersion relation $E(k)$ has a gap of $2\Delta = 2t(1 - \gamma)$. This configuration is the so called trivial and an energy gap appears in the dispersion relation.

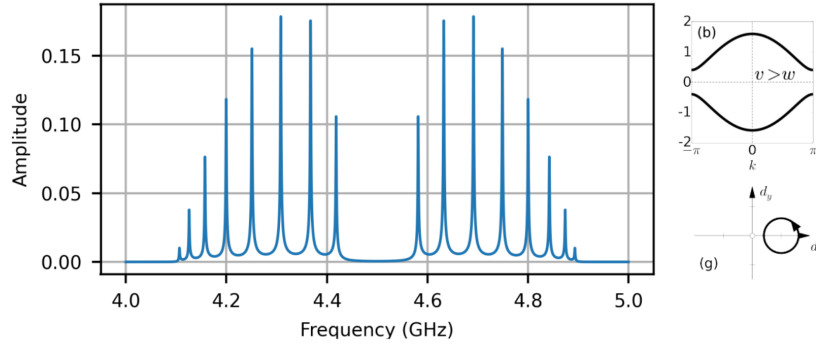


Figure 3.7: Trivial configuration; on the left the transmitted power is shown [23]; on the right dispersion relations and representation in d_x, d_y plane [3]

Topological Configuration The most interesting configuration happens once $\gamma > 1$, hence when inter cell hopping amplitude is larger than the intra cell term. Two main results arise from such configurations: On one side a band gap open, of size: $2\Delta = 2t(1 - \gamma)$. On the others side an interesting phenomena occurs in terms of edge states: the boundary of the chain hosts two edge states; located at right and at the left end of it, called in the following $|R\rangle$ and $|L\rangle$ with energy $E = e^{-N/\phi}$ with $\phi = 1/\log(\gamma)$ being the localisation length. Such an energy is located in the middle of the band gap and the edge state decay exponentially in the middle of the chain.

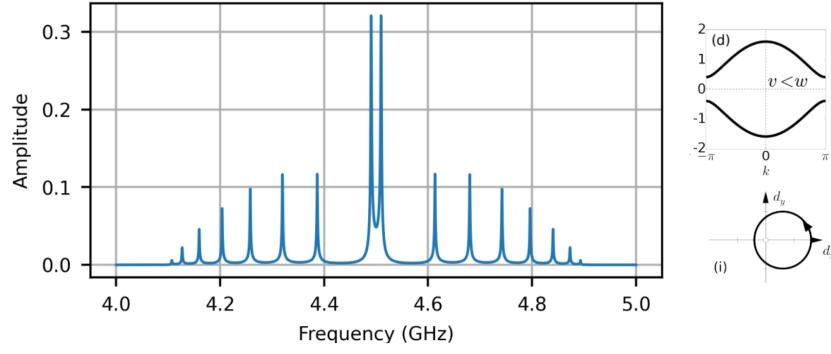


Figure 3.8: Topological configuration; on the left the transmitted power is shown [23]; on the right dispersion relations and representation in d_x, d_y plane [3]

The exponential decay result in small overlap and hybridisation resulting in symmetric and antisymmetric superposition:

$$|\Psi_{sym}\rangle = \frac{1}{\sqrt{2}}(e^{-i\phi/2}|L\rangle + e^{i\phi/2}|R\rangle) \quad (3.19)$$

$$|\Psi_{anti}\rangle = \frac{1}{\sqrt{2}}(e^{-i\phi/2}|L\rangle - e^{i\phi/2}|R\rangle) \quad (3.20)$$

This appears as available states in the middle of the band gap.

3.1.3. Qubit - Single Cavity interaction: Jaynes-Cummings model

As described in the previous chapter, the transmon qubit can be efficiently described as an anharmonic quantum oscillator with the following Hamiltonian:

$$\hat{H}_q = -\frac{\omega_q}{2}\sigma_z \quad (3.21)$$

or written by means of raising and lowering operators:

$$\hat{H}_q = \omega_q(\sigma_- \sigma_+ + \frac{1}{2}) \quad (3.22)$$

The qubit Hamiltonian by itself has two eigenstates $|\uparrow\rangle, |\downarrow\rangle$, corresponding to the two eigenvalues $\pm\omega_q/2$. In the same way, a single cavity mode Hamiltonian has an infinite number of eigenstates $|n\rangle$ with eigenvalues $\omega_c(n + 1/2)$ corresponding to n photons in that mode [16].

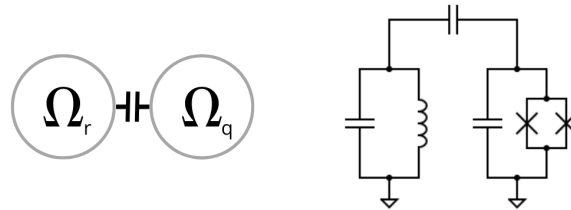


Figure 3.9: Schematic representation and equivalent circuit of a transmon qubit coupled to a resonator. The schematic shows the SQUID junction as non linear flux tunable element

It's now showed what the eigenstates and eigenvalues of the hybrid system through the interaction Hamiltonian are. The total Hamiltonian can be than written as follow:

$$\hat{H} = \omega_r(\hat{a}^\dagger \hat{a} + \frac{1}{2}) - \frac{\omega_q}{2}\sigma_z - g(\hat{a}^\dagger + \hat{a})(\sigma_- + \sigma_+) \quad (3.23)$$

If qubit and resonator are no interacting ($g = 0$), the eigenstates of the hybrid system would be the tensor product of the two systems eigenstates: $|\downarrow\rangle|n\rangle, |\uparrow\rangle|n\rangle$, with eigenvalues given by the sum of the two separate systems eigenvalues. We are instead interest in showing the effect of the coupling; Rewriting the Hamiltonian after the common practically justified RWA, the Hamiltonian is now written as:

$$\hat{H} = \omega_r(\hat{a}^\dagger\hat{a} + \frac{1}{2}) - \frac{\omega_q}{2} - g(\hat{a}^\dagger\sigma_- + \hat{a}\sigma_+) \quad (3.24)$$

The infinite number of eigenstates $|n\rangle$ force us to deal with an infinite dimension Hilbert space, leading to the following Hamiltonian representation through a semi infinite matrix:

$$H_{r,q} = \begin{pmatrix} \omega_r/2 - \omega_q/2 & 0 & 0 & \cdots & 0 \\ 0 & 3\omega_r/2 - \omega_q/2 & g & \cdots & 0 \\ 0 & g & 3\omega_r/2 + \omega_q/2 & \cdots & 0 \\ \vdots & \vdots & \ddots & \vdots & \\ 0 & 0 & \cdots & 0 & (n+1/2)\omega_r/2 + \omega_q/2 \end{pmatrix}$$

The general block of such Hamiltonian is in the form:

$$H_{r,q_n} = \begin{pmatrix} (n+1/2)\omega_r/2 - \omega_q/2 & \sqrt{n+1}g \\ \sqrt{n+1}g & (n+1/2)\omega_r/2 + \omega_q/2 \end{pmatrix}$$

Such representation takes into account of the transition between the eigenvalues n and $n-1$. This can be thus ulterior simplified by considering $n = 0$ and considering energy transition of a net quantity ω_q , leading to the following:

$$H_{r,q_n} = \begin{pmatrix} \omega_r & g_{r,q} \\ g_{r,q} & \omega_q \end{pmatrix}$$

The eigenvalues of the system are those related to the system ground state and those of $H_{r,q}$:

$$E_g = -\Delta/2 \quad (3.25)$$

$$E_{\pm} = (n+1)\omega_c \pm 1/2\sqrt{4g^2(n+1) + \Delta^2} \quad (3.26)$$

where $\Delta = \omega_q - \omega_c$ is the frequency detuning between qubit and resonator.

This show that the hybrid system generates an infinite set of eigenvalues; for every n , two hybridised eigenvalues will be present, spatially separated by a coupling and detuning dependent parameter. The eigenstate associated to those

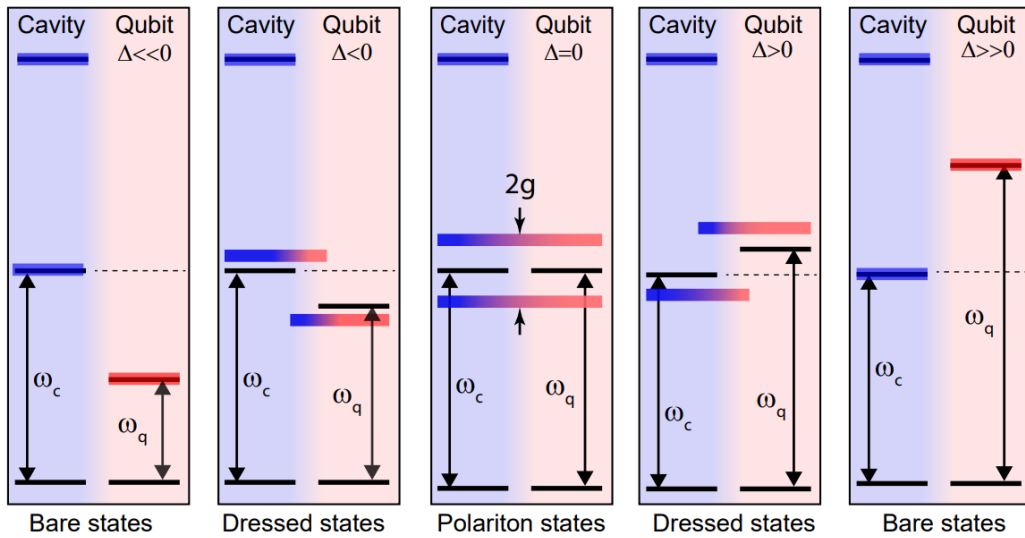


Figure 3.10: Schematic representation of the eigenvalues hybridization for a qubit coupled to single cavity. [16]

eigenvalues are called dressed state of the qubit and cavity:

$$|0, -\rangle = |g\rangle |0\rangle \quad (3.27)$$

$$|n, -\rangle = \cos(\theta_n) |g\rangle |n+1\rangle - \sin(\theta_n) |e\rangle |n\rangle \quad (3.28)$$

$$|n, +\rangle = \sin(\theta_n) |g\rangle |n+1\rangle + \cos(\theta_n) |e\rangle |n\rangle \quad (3.29)$$

this show that qubit and resonator hybridised their state, in a superposition of weighted by $\theta_n = \tan^{-1}(2g\sqrt{n+1}/\Delta)$. For $\Delta = 0$ the qubit and resonator frequency are matched, $\theta_n \rightarrow \pi/4$ and the dressed states go in maximum hybridization:

$$|n, \pm\rangle = \frac{1}{\sqrt{2}}(|g\rangle |n+1\rangle \pm |e\rangle |n\rangle) \quad (3.30)$$

These state are the so called polaritons and they differ for an energy $= 2g$. Once qubit level crosses the cavity levels, avoid crossing and hybridization appears.

Qubit state read out: Dispersive approximation If qubit and resonator are far detuned ($\Delta \gg g$), the interaction among those is relatively weak; in such condition the Hamiltonian in the dispersive limit can be written as:

$$\hat{H}_{dis} = \omega_c a^\dagger \hat{a} - \frac{1}{2} \omega_q \sigma_z - \frac{g^2}{\Delta} \hat{a}^\dagger \hat{a} \sigma_z \quad (3.31)$$

or eventually rearranged in a more clear format:

$$\hat{H}_{dis} = (\omega_c - \chi \sigma_z) \hat{a}^\dagger \hat{a} - \frac{1}{2} \omega_q \sigma_z \quad (3.32)$$

where $\chi = g^2/\Delta$ is the dispersive shift.

Is clear from this that the dispersive interaction is manifested as a qubit-state dependent frequency shift [16] for the resonator. If the qubit is the ground state, $|g\rangle$ then $\langle \sigma_z \rangle = 1$, thus the resonator frequency shift by $+\chi$; this phenomenon is fundamental, since it allows to determine the qubit state by detecting the read out resonator resonance frequency shift.

Qubit driving This section is dedicated to the investigation of the dynamic of a driven qubit; in this, a coherent light with Electric field in the form: $E(t) = E \cos(\omega_d t)$ is made interact with the qubit.

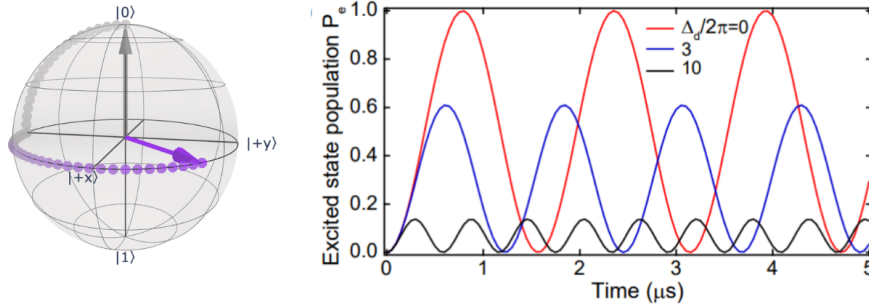


Figure 3.11: On the left, Bloch sphere representation for the qubit state evolution, on the right, time trace of the excited state population trend.[6]

The Hamiltonian of the two level system coupled to the external electric field, writes as follow:

$$H = -\omega_q \sigma_z / 2 - E(t) \hat{d} \quad (3.33)$$

where the second term is the interaction Hamiltonian, with $d = \vec{d} \sigma_x$ being the qubit electric dipole moment. searching for a solution to Schrodinger equation in the form:

$$|\psi(t)\rangle = C_g(t) e^{i\frac{\omega_q t}{2}} |g\rangle + C_e(t) e^{-i\frac{\omega_q t}{2}} |e\rangle \quad (3.34)$$

it is found that the complex coefficient, after the application of the rotating wave approximation, can be written as:

$$C_g(t) = \frac{e^{-i\Delta_d t/2}}{\Omega_r} (\Omega_r \cos(\Omega_r t/2) + i\Delta_d \sin(\Omega_r t/2)) \quad (3.35)$$

$$C_e(t) = i \frac{A e^{+i\Delta_d t/2}}{\Omega_r} \sin(\Omega_r t/2) \quad (3.36)$$

with $\Delta_d = \omega_q - \omega_d$ being the detuning between the qubit and driving signal and $\Omega_r = \sqrt{A^2 + \Delta_d^2}$ and $A = Ed$. It is interesting to look for an example at the population of the qubit excited state:

$$P_e(t) = |C_e(t)|^2 = \frac{A^2}{\Omega_r^2} \sin^2(\Omega_r t/2) \quad (3.37)$$

As shown in Fig. 3.11 (right) The qubit can than be fully rotated from the ground to the excited state by an on-resonance external drive, simply by controlling how strong and how long the drive have to last.

3.2. Qubit coupled to single and multimode system

The coupling between a multi-mode metamaterial and a single transmon qubit in different configurations is now investigated:

3.2.1. Transmon qubit coupled to single resonator in a metamaterial

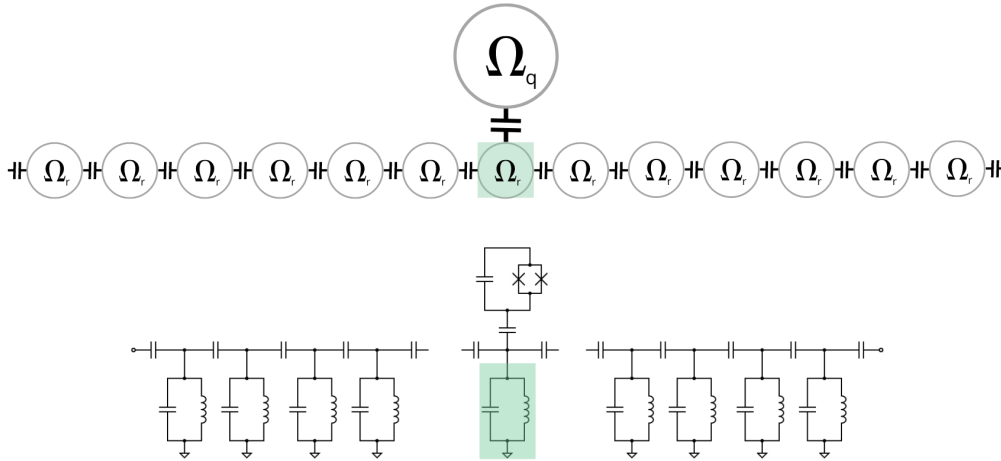


Figure 3.12: Schematic and equivalent circuit of two level system coupled to single resonator of a cavities array.

The Hamiltonian of the coupled system can be written as follow:

$$\hat{H}_{mm,q} = \sum_i \omega_{R_i} (\hat{a}_i^\dagger \hat{a}_i + \frac{1}{2}) + \sum_{i,j} g_{r_i,r_j} (\hat{a}_i^\dagger \hat{a}_j + \hat{a}_i \hat{a}_j^\dagger) - \frac{\omega_q}{2} \sigma_z - g_{r_m,q} (\hat{a}_m^\dagger \sigma_- + \hat{a}_m \sigma_+) \quad (3.38)$$

which translate into the following matrix formulation:

$$H_{m,m} = \begin{pmatrix} \omega_{r1} & g_{r1,r2} & \cdots & \cdots & \vdots & g_{r1,rn} \\ g_{r1,r2} & \omega_{r2} & \cdots & \cdots & \vdots & g_{r2,rn} \\ \vdots & \vdots & \ddots & g_{rm,q} & \vdots & \vdots \\ g_{r1,rm} & \cdots & g_{rm,q} & \omega_q & \vdots & \vdots \\ \vdots & \vdots & \vdots & \vdots & \ddots & \vdots \\ g_{rn,r1} & g_{rn,r2} & \cdots & \cdots & \cdots & \omega_{rn} \end{pmatrix}$$

From the Hamiltonian formulation it can be seen that the coupling to the two level system introduce a new engineerable term in the off diagonal in the correspondence to the coupling site. By diagonalizing the Hamiltonian and computing the system's eigenvalues while varying the qubit frequency ω_q , Fig. 3.13 are obtained.

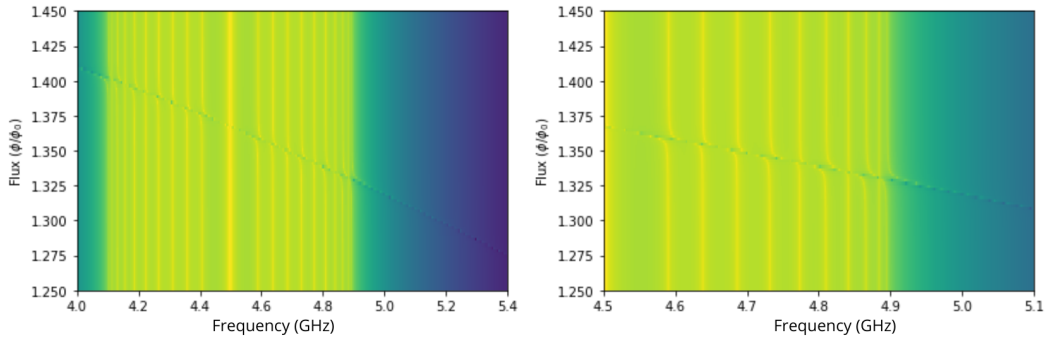


Figure 3.13: Eigenvalues plots for the Hamiltonian of transmon qubit coupled to single mode; avoided crossing is shown.

The avoided crossing described in the previous section can be observed as an indicator of the qubit coupling with individual modes of the system.

3.2.2. Atom-photon bound state

Qubit strongly coupled to a multimode photonic environment give rise to qubit-photon dressed bound state. [22] The bound photonic state spatially localize around the atom, exponentially decaying in an envelope that tunes with detuning of the qubit transition from the band edge. The frequency of the bound state changes with qubit frequency, and become less localized as the bare qubit it tuned closer to the band edge.

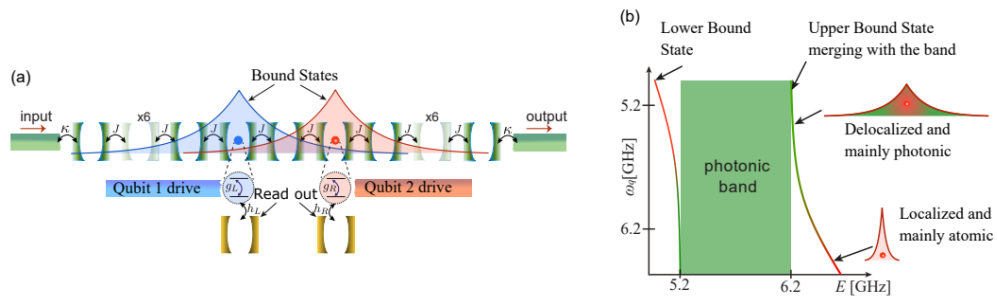


Figure 3.14: Schematic representation of the atom-photon bound state phenomenon; Once the qubit frequency approaches slow photon modes, such as edges mode, the spatial photonic distribution is localized around the qubit.[20]

Once the qubit frequency approaches the band edge mode, the large atom-photon spatial localization, allow to facilitate the photon transmission along the metamaterial at the bound state frequency; this allows for tunable photonic interaction mechanism. As the localization length increases, the line-width of the signal increases, allowing for the detection of the change in wave function overlap.[20]

Atom photon bound state in single mode coupling

From the set of eigenstates derived from the previous Hamiltonian, the spatial photons distribution can be obtained and plotted as function of the detuning between the qubit and the band edge mode, resulting in Fig. 3.15

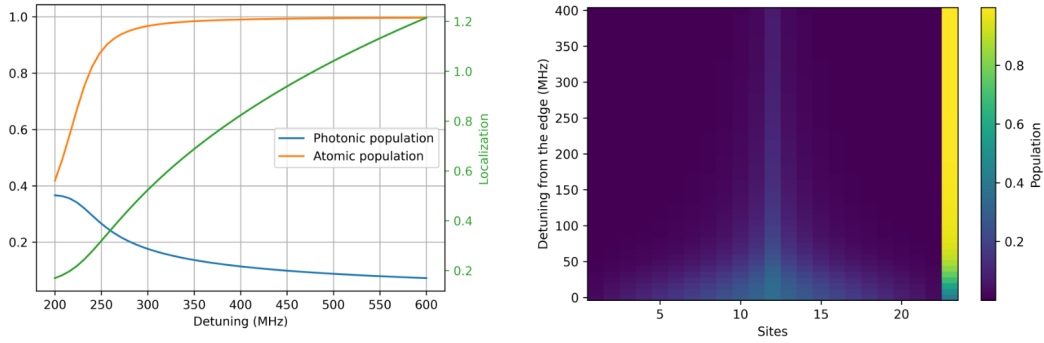


Figure 3.15: The figure on the right shows the spatial photon distribution in the metamaterial as function on the qubit - band edge detuning; figure on the left shows a cross section of it.

3.2.3. Transmon qubit coupled to multiple resonators in a metamaterial

Uniform Coupling to K-resonators

In this section investigates the interaction of a single transmon qubit to multiple resonator of a multi mode metamaterial made out of N coupled resonators; in first place only the interaction between the transmon and a set of $K < N$ resonators will be considered.

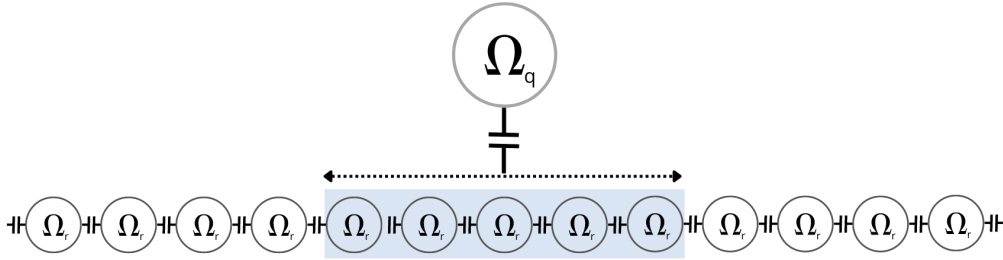


Figure 3.16: Schematic and equivalent circuit of two level system coupled to multiple resonator of a cavities array.

The Hamiltonian of the coupled system can be written as follow:

$$\hat{H}_{mm,q} = \sum_i \omega_{R_i} (\hat{a}_i^\dagger \hat{a}_i + \frac{1}{2}) + \sum_{j,i} g_{r_i,r_j} (\hat{a}_i^\dagger \hat{a}_j + \hat{a}_i \hat{a}_j^\dagger) - \frac{\omega_q}{2} \sigma_z + \sum_k^K g_{r_k,q} (\hat{a}_k^\dagger \sigma_- + \hat{a}_k \sigma_+) \quad (3.39)$$

which translate into the following matrix formulation:

$$H_{m,m} = \begin{pmatrix} \omega_{r1} & g_{r1,r2} & \cdots & \cdots & \vdots & g_{r1,rn} \\ g_{r1,r2} & \omega_{r2} & \cdots & 0 & \vdots & g_{r2,rn} \\ g_{r1,rk_1} & \cdots & \cdots & g_{rk_1,q} & \vdots & \vdots \\ \vdots & \vdots & \ddots & g_{rm,q} & \vdots & \vdots \\ g_{r1,rn} & 0 & g_{rm,q} & \omega_q & \vdots & \vdots \\ \vdots & \vdots & \vdots & \vdots & \ddots & \vdots \\ g_{rn,r1} & g_{rn,r2} & \cdots & \cdots & \cdots & \omega_{rn} \end{pmatrix}$$

By diagonalizing the Hamiltonian and computing the system's eigenvalues while varying the qubit frequency ω_q , Fig. 3.17 are obtained.

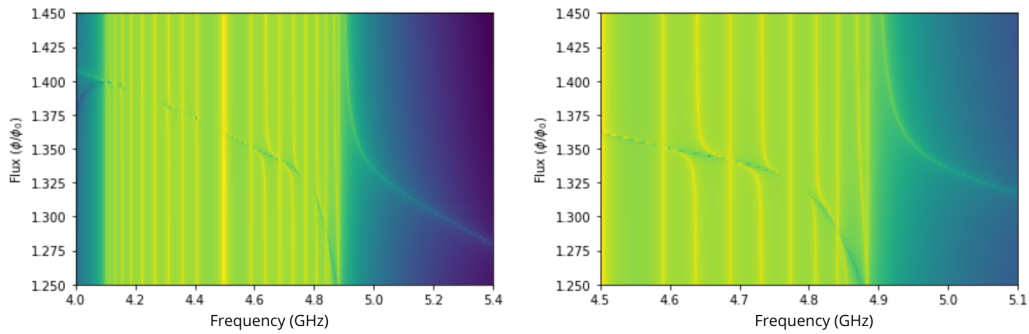


Figure 3.17: Schematic and equivalent circuit of two level system coupled to multiple resonator of a cavities array.

In opposition to the single mode coupling, different effect is observed in this case; the qubit does not couple uniformly to all the metamaterial modes. This is a result deriving from the multiple site coupling; the spatial photon distribution in correspondance of the qubit overall location (as can be seen from the eigenstates distributions), leads to a net coupling that cancel out in some of the metamaterial modes; this has been shown and experimentally demonstrated as described in the next sections.

Atom photon bound state in multi mode coupling

From the set of eigenstates derived from the previous Hamiltonian, the spatial photons distribution can be obtained and plotted as function of the detuning between the qubit and the band edge mode, resulting in Fig. 3.18

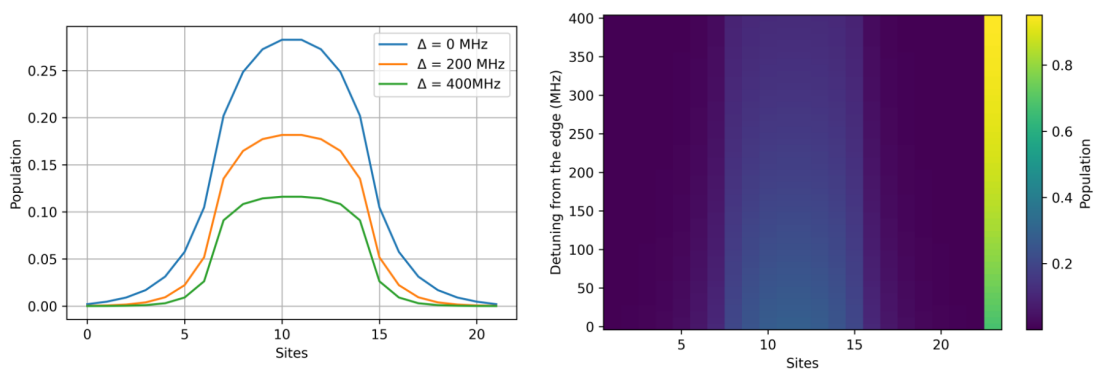


Figure 3.18: The figure on the right shows the spatial photon distribution in the metamaterial as function on the qubit - band edge detuning; figure on the left shows a cross section of it. With the respect to the previous section the transmon is coupled to eight site of the metamaterial.

As can be seen also in this case, the photon distribution exponential localization changes with the the qubit - band edge detuning.

Uniform Coupling to K-resonators and coupling to N-K metamaterial resonators

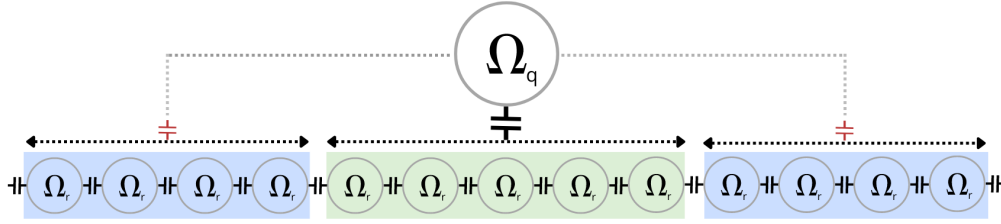


Figure 3.19: Schematic and equivalent circuit of a complete realistic model for a two level system coupled to multiple resonator of a cavities array. Both direct coupling to site of interest and non is taken into account.

In this section we will model the interaction of a single transmon qubit to multiple resonator of a multi mode metamaterial made out of N coupled resonators; the transmon will strongly interact with every resonator $r_k i$ over set of $K < N$ resonators, and weakly to every resonator $r_k z$ over set of $Z = N - K$ resonators

The Hamiltonian of the coupled system can be written as follow:

$$\hat{H}_{mm,q} = \sum_i \omega_{R_i} (\hat{a}_i^\dagger \hat{a}_i + \frac{1}{2}) + \sum_j g_{r_i,r_j} (\hat{a}_i^\dagger \hat{a}_j + \hat{a}_i \hat{a}_j^\dagger) - \frac{\omega_q}{2} \sigma_z + \sum_k^K g_{r_k,q} (\hat{a}_k^\dagger \sigma_- + \hat{a}_k \sigma_+) + \sum_{z \neq k}^{N-K} g_{r_z,q} (\hat{a}_z^\dagger \sigma_- + \hat{a}_z \sigma_+) \quad (3.40)$$

which translate into the following matrix formulation:

$$H_{m,m} = \begin{pmatrix} \omega_{r1} & g_{r1,r2} & \cdots & \cdots & \vdots & g_{r1,rn} \\ g_{r1,r2} & \omega_{r2} & \cdots & \cdots & \vdots & g_{r2,rn} \\ g_{r1,rk_1} & \cdots & \cdots & g_{rk_1,q} & \vdots & \vdots \\ \vdots & \vdots & \ddots & g_{rm,q} & \vdots & \vdots \\ g_{r1,rm} & \cdots & g_{rm,q} & \omega_q & \vdots & \vdots \\ \vdots & \vdots & \vdots & \vdots & \ddots & \vdots \\ g_{rn,r1} & g_{rn,r2} & \cdots & \cdots & \cdots & \omega_{rn} \end{pmatrix}$$

This section is fundamentally analogous to the previous formulation; it has been added to show a more realistic model.

4

A device to achieve analog quantum simulation

In the following chapter will be highlighted a platform thought to experimentally achieve analog quantum simulation of a bosonic environment coupled to an artificial atom.

4.1. Design approach

The design has been realized by python coding, mostly using the library gdsapy; such library allow to efficiently design multi-layer structures, generating a .gds file containing the thought design.

4.1.1. General Overview

The main "ingredients" needed to achieve the realization of a device for the experimental demonstration of the previously introduced phenomena are:

- An engineered microwave environment, such to emulate the behavior of a bosonic environment
- An artificial atom, capable of interacting, and hybridizing with the multi-mode system.

The following figure briefly schematizes the main idea and the main features that must belong to the device.

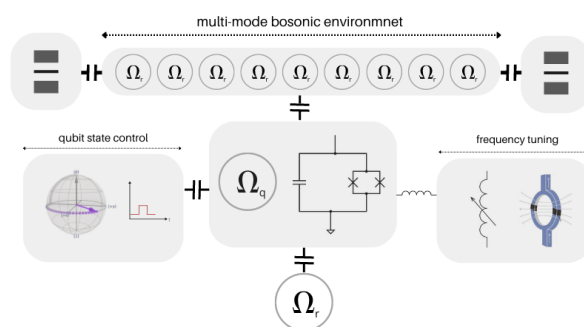


Figure 4.1: Schematic overview of the intended device: A multi mode system is capacitively coupled to a transmon qubit. The two level system resonance frequency is tunable by a magnetic flux through the DC line; the state is addressable by the feedline and readable by the read out resonator, hanged on the bottom waveguide.

4.1.2. Superconducting multi-mode metamaterial

The realization of a bosonic environment required the implementation of a cavity, capable to "trap" standing waves on its inside. Such waves must be in the order of the few GHz, in this case ranging in the interval: [4GHz,10GHz].

Single resonator

As previously described, the metamaterial is composed of the series of N lumped cavities, coupled through a certain coupling g_k . The single cavity is described, for than generalizing the concept to N coupled resonators. As already mentioned, the multimode spectrum is achieved by making interact a certain number of equivalent LC resonators, all with the same resonant frequency: ω_r ; the resulting hybridisation allows for the creation of the microwave environment. Let's suppose the resonant frequency wanted is in the order of $\omega_r = 5GHz$. The resonant frequency of a simple lumped oscillator can be written as follow:

$$\omega_r = \frac{1}{2\pi\sqrt{L_r C_r}} \quad (4.1)$$

From such first equations, a simple first problem can be noticed: The target of a resonance frequency of the order of 5GHz, by means of the intrinsic inductance of the most common superconducting materials, would require capacitances of the order of few hundreds of fF. This results in extremely large resonators, limiting the scalability of the final device, which require the coupling of tens of cavities. Such first issue is solved by means of a very well know property of many superconducting material: **Kinetic Inductance**. By sputtering a thin film (20nm) of superconducting Niobium Nitride(NbN), an inductance of 90nH/ \square is reached, allowing for the realization of ultra compact resonators. The following figure shows the implementations of a single metamaterial's resonators and different attempted configurations.

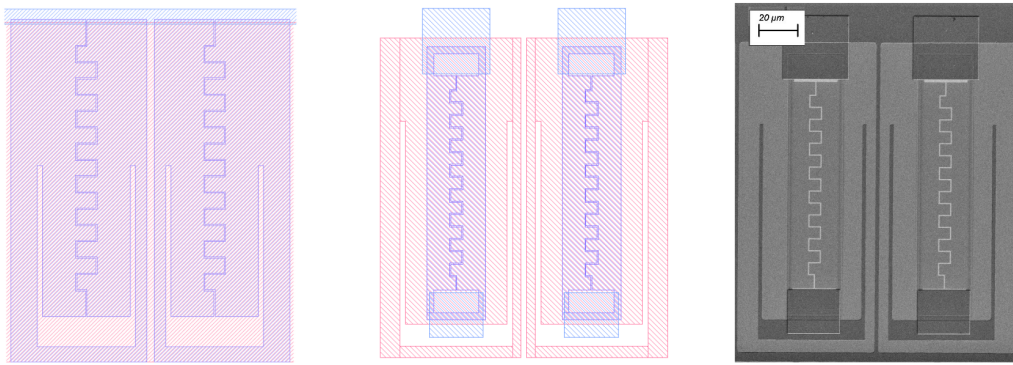


Figure 4.2: Lumped element resonator; individual element of the metamaterial. The capacitive inter coupling is obtain through the Aluminum body, while the high inductance is obtained through the NbN inductor.

The main challenge in the realization of such resonators is the integration of a high kinetic inductance film, into an Aluminum ground plane; such a need derives from the attempt to take advantages of the main features of each of these materials. On one side, the high kinetic inductance allow to realized extremely compact resonators, on the other side, the superconducting Aluminum allows for the realization of high quality, magnetic flux insensitive devices.

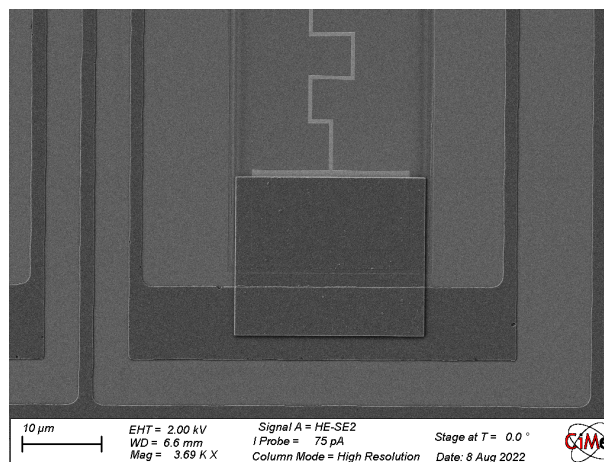


Figure 4.3: The NbN inductor is patched on the Aluminum ground plane to ensure electrical contact

Being the main target of this platform the attempt to characterize the interaction of flux tunable qubit with an array of ultra compact cavities, perfect diamagnetism must be achieved; if not, the application of a magnetic field, would result in the formation of Abrikosov vortices and induced flux jumps due to the extremely sensitivity of SQUID loops.

The two resonators configurations depicts the attempted approaches. In the first configuration, the whole resonator is made out of dry etched NbN, patched to ground by 200nm of Al; Two main problems arise from such configuration: firstly, the resonator are only grounded by few μm overlapping between the inductor and the Aluminum ground plane.

In second place, the capacitive component of the resonator contribute to distributed inductance of the overall all resonator. To avoid such problems, the second resonator version has been realized, where a the capacitive component was made out of the wet etching of the Aluminum ground plane and the only inductive component was realized by NbN dry etching. This allowed to patch directly on top of the inductor ensuring a better grounding as depicted in figure.

Ghost resonators

The metamaterial is a periodic structure that needs every element of the array to have the same resonance frequency ω_r . The connection with the signal waveguide results to be critical in this; in fact it may introduce a resonance mismatch due to the different capacitive environment. To solve this problem, a "ghost" resonators is added at the two extremes of the metamaterial. Such resonator, in reality does not resonate in the spectrum of interest, being the inductor not shunted to ground. The utility of the ghost, is than to only mimic the capacitive environment, ensuring a resonance frequency match among all the resonators of the metamaterial.

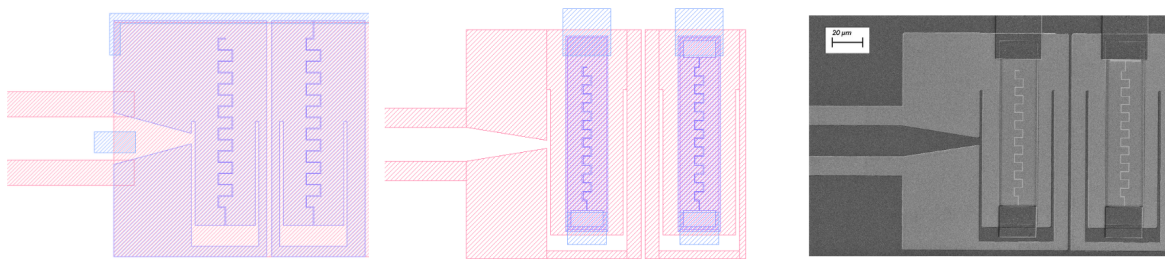


Figure 4.4: In order to ensure the same capacitive environment for all the resonator of the metamaterial, ghost resonators are added at the metamaterial termination,

As seen in the figure, the ghost resonators has been realized with the same concept in both the attempted design configurations.

Metamaterial

Combining the previously described resonators into an arbitrary long arrays of cavity, results in the formation of a superconducting metamaterial. In the following figure, the qubit capacitor can already be seen, coupled to the array.

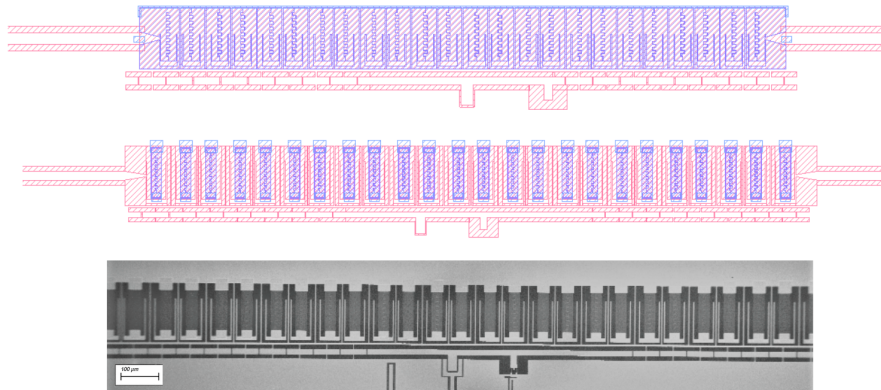


Figure 4.5: Design and SEM image of the final metamaterial

Such capacitor introduce a resonance mismatch in the qubit-metamaterial coupled resonators; to solve the issue, an array of compensating capacitors is added in the proximity of the uncoupled resonators, such to avoid any resonance mismatch, ensuring uniformity among the capacitive environment distribution. By properly engineering the coupling among resonators, different metamaterial working configuration can be achieved:

- Normal Configuration
- Trivial Configuration
- Topological Configuration

4.1.3. Transmon qubit

As previously explained, a transmon qubit is made out of a non linear LC resonator. Having said so, it looks at this point straightforward to realize a transmon qubit coupled to a cavity array, by a capacitive coupling and a SQUID junction shunted to ground as a non linear component.

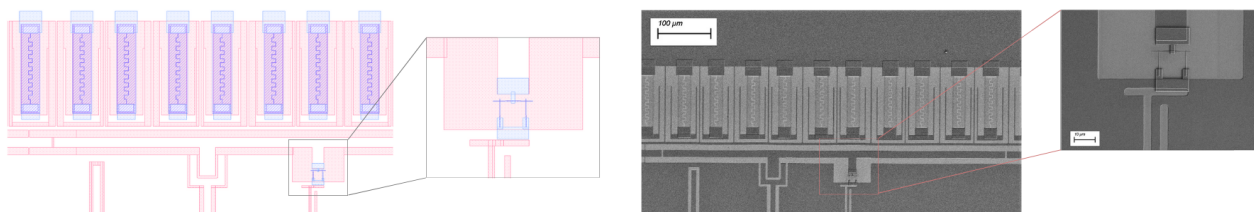


Figure 4.6: Design and SEM image of the transmon qubit coupled to metamaterial. In the figure it can be seen the NbN cavities array, the transmon body and the the termination of feedline, read out resonator and flux line.

In the figure, the intended design and an SEM images of the realized device are shown. The Al transmon body is capacitively coupled to 8 resonators of the metamaterial and shunted to ground by means of the SQUID junction.

SQUID junctions

As just mentioned, the SQUID junction represent the non linear element that ensure the transmon qubit anharmonicity and flux tunability. It is fabricated by Manhattan evaporation technique: First, the horizontal 180nm width line

is evaporated ,than a static oxidation the performed at 0.15 Torr, finally the two parallels 180nm width line are evaporated leading to the formation of two parallel Josephson Junction shunted to ground in a close loop.

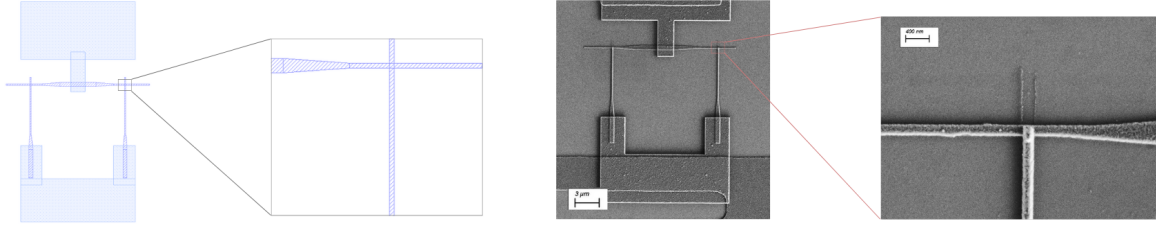


Figure 4.7: SQUID junction with zoom in on the Josephson junction

The qubit capacitance and inductance allow to reach a zero-flux resonance frequency located at approximately 7.5GHz.

4.1.4. Read-out resonator

Metamaterial and qubit components have been explained, now a brief of explanation of how to interact with them will be carried out. First of all, in order to be able to read out the state of the qubit, a read out coplanar waveguide resonator must be coupled to it. As can be seen the coupling is achieved directly in the transmon body with an U shape CPW such to reduce the occupied overall coupling area. The read out resonator implemented is a meandered $\lambda/4$ resonator. In such configuration, the resonator is inductively coupled to the bottom CPW waveguide (see Final device section), and capacitively coupled to the transmon body where the electric field concentration is at its maximum.

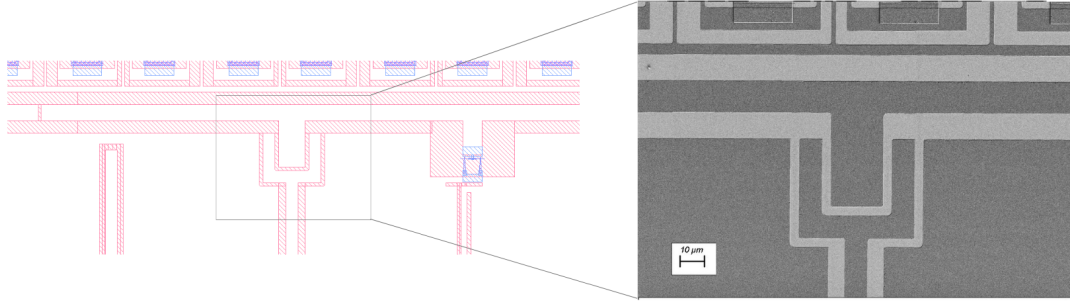


Figure 4.8: Read out resonator termination to ensure capacitive coupling between the transmon body and the read out resonator.

The resonance frequency of the CPW can be written as follow:

$$f_0 = c/(2L\sqrt{\epsilon_{eff}}) \quad (4.2)$$

where L is the overall resonator length.

The impedance is instead simply:

$$Z_0 = \sqrt{L/C} \quad (4.3)$$

The resonator has been designed to be 50Ω matched, and with a resonance frequency of 4.5 GHz. For what concern the coupling between CPW resonator and transmon body, it can be estimated as follow:

$$g_{ro,q} = \frac{1}{2}\omega_{ro}\omega_q C_c \sqrt{Z_q Z_{ro}} \quad (4.4)$$

where $C_c = 10$ fF is the coupling capacitance between the read out resonator and the qubit body, $Z_{ro} = 50\Omega$ is the read out resonator impedance and $Z_q = \sqrt{L_q/C_q}$ is the qubit impedance, with $C_q = 96$ fF.

4.1.5. Flux Line

In order to be able to flux tune the qubit frequency, a magnetic field must be applied in the proximity of the SQUID junction. The SQUID junction critical current can in fact be written as:

$$I_0^{SQUID} = 2I_0 \cos\left(\frac{\pi\phi_{ext}}{\phi_0}\right) \quad (4.5)$$

where I_0 is the critical current of the single Josephson junction.

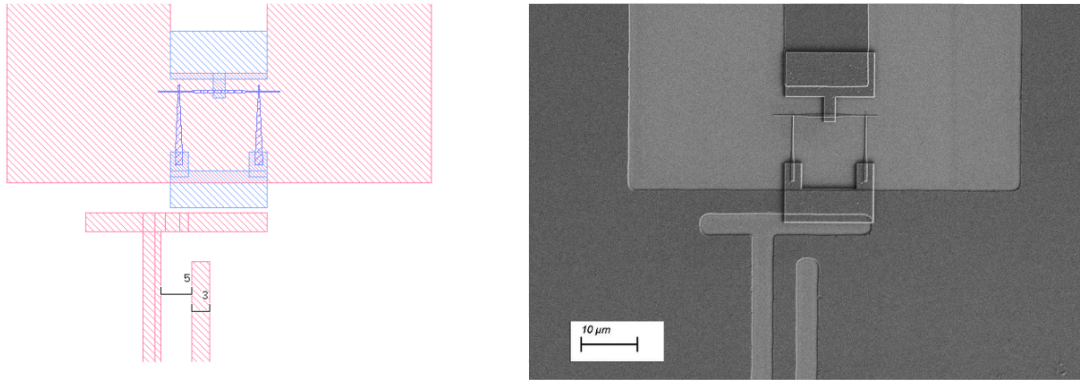


Figure 4.9: Flux line termination; it consists of a DC line shunted to ground that generates a magnetic field entering the SQUID loop and generating a change in the qubit resonance frequency.

By shunting to ground a DC line in the proximity of the SQUID loop, the current passing through it generates a magnetic field that modifies the inductance of the non-linear element, resulting in a downshift of the qubit resonance frequency; such features allow for the controlled hybridisation between the qubit and the different metamaterial modes.

4.1.6. Quantum State control feed line

As explained in the previous sections, in order to effectively control the quantum state of the qubit, a sequence of voltage pulses must be applied to the transmon body. The effect of pulse application can be visualized as a controlled rotation of the state vector in a Bloch sphere.

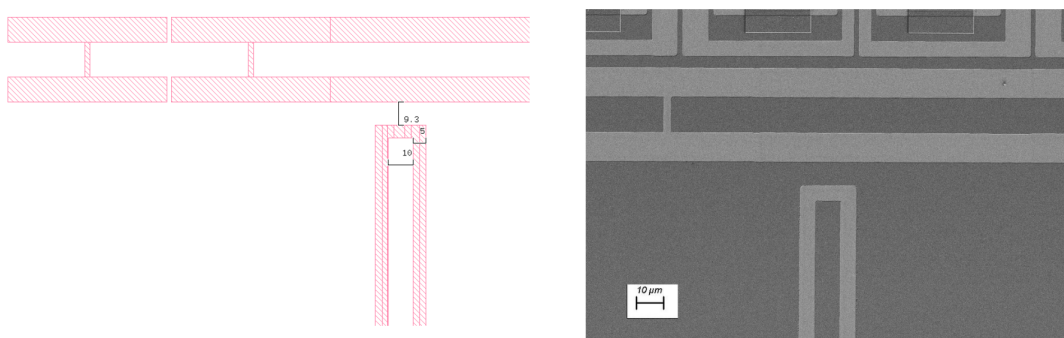


Figure 4.10: Feedline termination capacitively coupled to the transmon body. It consists of a CPW waveguide where time-domain signals are sent to control the qubit state.

The design simply consists of a 50Ω matched CPW waveguide, terminated with an open circuit such to maximise the electric field concentration in the proximity of the qubit body.

4.1.7. Final Design

The complete final device is composed as depicted in the following Figure.

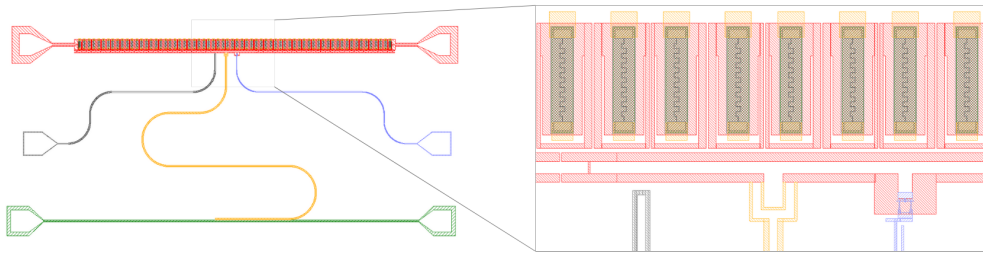


Figure 4.11: Final design: in red the metamaterial, in yellow the read out resonator, in blue the fluxline, in grey the fluxline, in green the waveguide to which read out resonator is hanged.

- In red is depicted the metamaterial with the associated waveguide and pads
- In yellow is shown the read out resonator, capacitively coupled to the transmon body on the top and inductively coupled to the waveguide on the bottom
- In green a simple CPW waveguide is design, such to measure in transmission the state of the read out resonator.
- In blue the flux line can be seen, externally connected to a DC source allows for the transmon qubit frequency tuning.
- In grey the CPW feedline, use to control the state of the qubit by the application of a time pulsed sequence

4.2. Validating the design by means of structural and behavioral simulations

In order to properly finalize the design, the static and dynamic behaviour of each component has been simulated, leading to a feedback in design modification such to ensure the correct final device functionalities.

4.2.1. Electrostatic simulations: capacitance distribution

The capacitance distribution is simulated for each single resonator, interacting with the surrounding environment. The

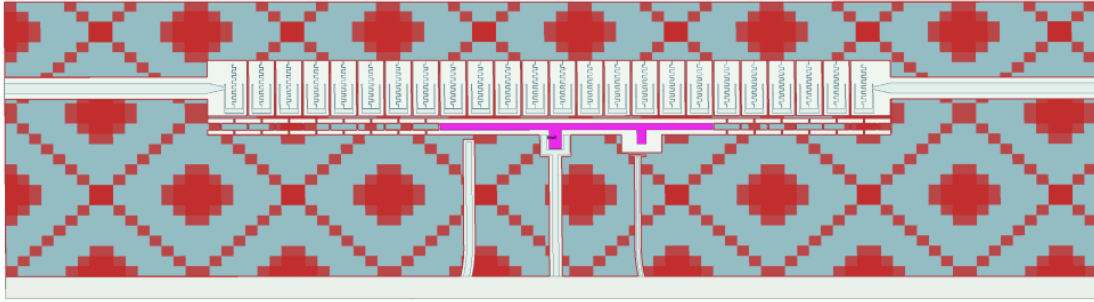


Figure 4.12: Schematic CAD of the design simulated on ANSYS to obtain the capacitance distribution of the system,

software used to perform this simulation is Ansys Electronics. The following figure show the outputted capacitance matrix; these values (expressed in fF) are used to simulate the exact behaviour of the system but taking into account all the coupling term g in system Hamiltonian.

As can be seen in Fig. 4.13, the capacitive environment for each of the metamaterial's resonators is managed to be maintain constant even with the insertion of the multiple site coupled transmon qubit. This show that the "fake"

r1	r2	r3	r4	r5	r6	r7	r8	r9	r10	r11
21.026	19.763	20.073	20.17	19.853	20.301	19.691	19.616	19.738	19.545	19.396
r12	r13	r14	r15	r16	r17	r18	r19	r20	r21	r22
19.897	20.257	19.666	20.061	19.724	20.055	20.13	20.323	19.927	19.775	19.884

Figure 4.13: Capacitance distribution for all the resonators in the metamaterial; all unit in fF

capacitor underneath the metamaterial works as expected flattening the overall resonators resonance frequency to a constant value of $\approx 20fF$.

It's now of fundamental importance to examine the capacitance distribution on the transmon surrounding. The overall capacitive coupling of $\approx 96fF$ fixes, together with the resulting SQUID inductance, the 0-flux transmon qubit resonance frequency.

	FeedLine	FluxLine	Ground	ReadOut	Total
Transmon	-0.35474	-0.18033	-72.726	-10.991	96.941

Figure 4.14: Capacitance distribution for the transmon qubit; all unit in fF

4.2.2. Dynamic simulations: Behavioural analysis

The system is then simulated dynamically by means of the software Sonnet. Through this simulation is possible to obtain the transmission spectrum S_{12} of the metamaterial and the resonances frequency of every element in the design.

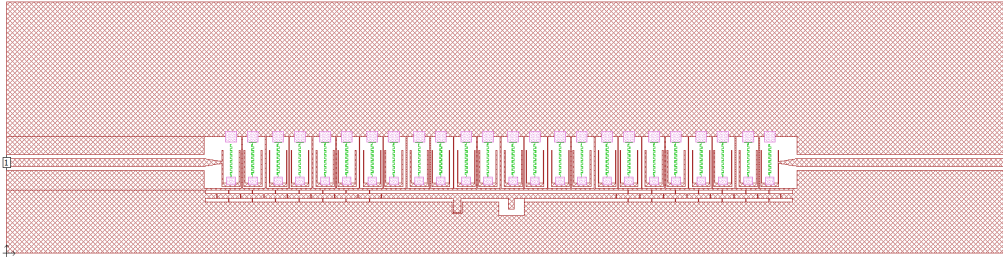


Figure 4.15: CAD showing the design simulated on Sonnet

By means of such simulation is also possible to obtain the current spatial distribution in the metamaterial for every mode of the system. This allow to have a final confirmation on the mathematical model and allow to predict in which of the multimode the transmon will exhibit higher coupling.

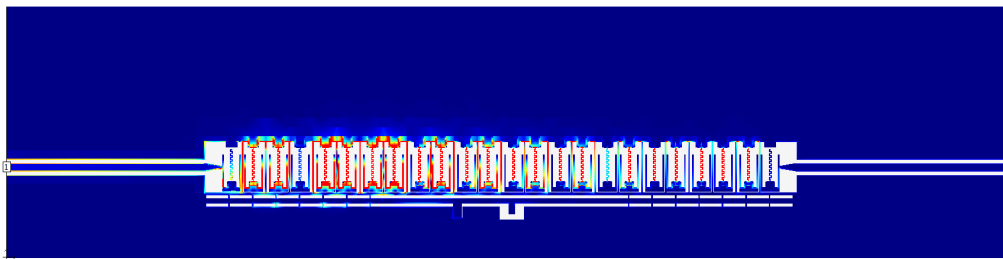


Figure 4.16: Sonnet simulation result in term of electric current distribution in the system for the 16th resonance mode

Engineering photonic band-gap - Transmission

The following shows an example of output results when computing the $|S_{21}|^2$ spectrum for a metamaterial in normal configuration.

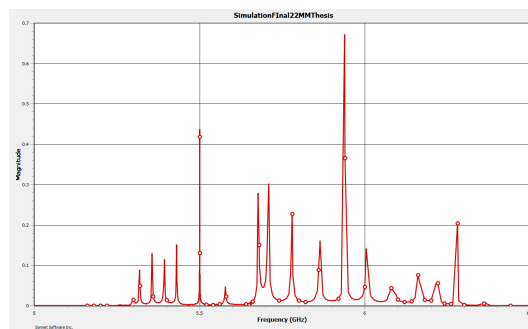


Figure 4.17: $|S_{21}|^2$ resulting from Sonnet simulation in linear scale

This simulation allows to have a final confirmation about the model correctness; the device fabrication is described in the following chapter.

5

Device fabrication - Process Flow in details and alternatives solutions

5.1. The need of a platform - Investigating possible alternative

In the following a detailed description of the accomplished fabrication will be presented; The whole process has been carried out in EPFL's Center of MicroNanoTechnology (CMi) cleanroom and EPFL's Physics department clean room. Each process flow step will be described in detailed and different approaches will be presented.

The main target of this section is to investigate a stable, reproducible fabrication process aiming to realize a platform for the quantum analog simulation of the ultra strong interaction between an artificial giant atom modeled as a two level system, and a microwave multimode bosonic environment, realized by mean of a superconducting high kinetic inductance metamaterial.

In order to obtain an efficiently working platform, different materials must be combined in the same process aiming to extract the best overall performance: high kinetic inductance, non linear Niobium Nitrite is used to realize the superconducting metamaterial; Such right-handed metamaterial is composed of an array of coupled LC resonator; sputtered NbN allow to achieve extremely high and controllable kinetic inductance per square, allowing for a notable scaling in resonators dimension, still working in the GHz regime. Nonetheless Niobium Nitride is a disordered type 2 superconductor, which results in the formation of Abrikosov vortexes under the application of a magnetic field. The cooper-pair Box superconducting qubit has an in inductive flux tunable component given by the SQUID junction, allowing for the study of the interaction with different modes of the bosonic environment. SQUID junction inductance is the most sensible magnetometer, sensible to magnetic flux quanta; such feature results to be quite incompatible every time a device is subjected to the application of magnetic fields; the formation of Abrikosov vortices result in uncontrollable inductance changes and resulting qubit frequencies jumps.

To overcome this issue the overall structure, except the superconducting metamaterial, has been made out of a type 1 superconductor: Aluminum.

5.2. Platform fabrication processes - Detailed Description

The figure shows part of overall process flow, tough to achieve the desired result.

The substrate used for the realization of the platform is a 2 inches, $280\mu\text{m}$ thick, high resistive silicon wafer.



Figure 5.1: 2 inches, high resistive silicon wafer, covered by native silicon oxide

To clean the surface from the native oxide, an RCA cleaning is performed, or alternatively a room temperature hydrofluoric acid 1% bath is performed for 5 minutes in 250mL volume; successively the wafer is rinsed in two bath of deionized water, 5 minutes each, such to ensure the absence of HF residual on the wafer surface[b].

The material used for the realization of the

- readout coplanar waveguide (CPW) superconducting resonator
- frequency tuning flux line
- qubit state drive line
- transmission read out coplanar waveguide

is, for the reasons briefly described previously, Aluminum. Being the Aluminum the main element used in the realization of the device, the deposition of the last results to be a crucial step in the overall performances, in term of quality factor, losses and repeatability. High purity, good adhesion, grain size must be controlled accurately to achieve best performances.

The tool used for the evaporation of the Aluminum is the Plassys MEB550SL3; such tool is an ultra high vacuum e-beam evaporator that allow to evaporate from up to 8 different crucibles, maintaining the evaporation chamber pressure at 10^{-10} Torr, by mean of a cryogenic pump. Additionally such tool is composed as multi-chamber system made of 3 independent, isolated chamber: A chamber for the wafer insertion, ozone generation and ion milling, a chamber entirely dedicated to ultra high vacuum evaporation and a chamber dedicated to static and dynamic oxidation by controlling the flux of oxygen in the chamber. As explained in the SQUID junction realization sub-chapter, such feature will be crucial for allowing the realization of Josephson Junction without "breaking" the vacuum.



Figure 5.2: Silicon wafer after native oxide removal

Going back to the process flow; the wafer, which surface has just been cleaned from the native oxide, is now, as fast as possible, to reduce the amount of native oxide formation, loaded in the load-lock of the UHV evaporator, which pressure is immediately pumped down to 10^{-6} Torr to stop the SiO_2 formation.

The wafer is than transferred in the evaporation chamber, the pressure is pumped to 10^{-10} Torr and 2nm of Titanium are evaporated at shutter close such to absorb all oxygen residual in the chamber. By means of e-beam evaporation, 150 nm of Al are than evaporated, forming the ground plane of the device[c]. The wafer is than finalized by static oxidizing the Al at 4 Torr for 10 minutes leading to the growth of a SiO_2 passivation layer of known properties.

The following step is the markers patterning and evaporation.

Markers will allows for the correct alignment of the different layer of the process flow. The patterning is performed by mean of the Electron beam lithography system: Raith EBPG5000+.



Figure 5.3: Aluminum coating in UHV evaporator for ground plane

The wafer is coated with a double layer of methyl methacrylate (MMA) and poly methyl methacrylate (PMMA); both are positive e-beam resists consisting of long polymer chain of carbon atoms but with different molecular weight. Such difference in molecular weight is the key to achieve a proper undercut, which allow to perform lift-off limiting the deposition along the side wall.

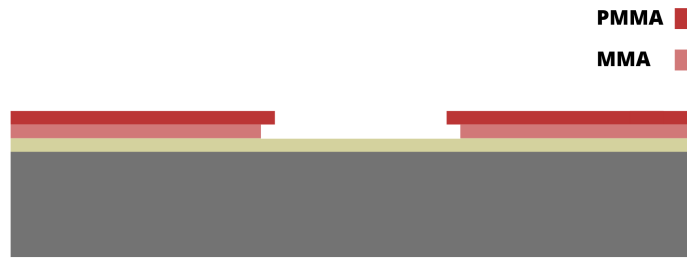


Figure 5.4: Bi-layer of MMA/PMMA; e-beam resist to obtain undercut allowing for efficient lift-off

The MMA has a lower molecular weight than PMMA, this results in a faster developing rate and the formation of the under cut showed in figure.

For the markers patterning, the wafer is first thermally dehydrated for 5min at 180°C, is then coated with a first layer of 200nm of MMA EL6, manually spin coated at 2000rpm. The first resist layer is then soft baked at 180°C for 5 min to harden the resist evaporating the solvent. The second resist layer of PMMA 950 A2 is then spin coated at 2000 rpm to achieve a thickness 100nm. The same soft-baking procedure is repeated by heating the wafer on a hot plate for 5 min at 180°C [d].



Figure 5.5: Wafer coating with MMA/PMMA for markers definition

The wafer is now loaded inside the e-beam system load-lock. Transferred in the exposure chamber the resist is exposed according to the following: Markers are exposed with Dose = 1200, Pixel = 40, Beam current = 100nA; Spacers are exposed with Dose = 1000, Pixel = 80, Beam current = 200nA;

Where Spacers refers do the patterning of the dicing lines, useful as a reference for line cut along during the dicing process to obtain the different dies.

The choice of such parameters is such to optimize the trade-off between writing frequency and maximum resolution. The optimal dose is obtain through a previous dose-test, than pixel size and beam diameter are obtained by taking into account that writing frequency is obtained as follow:

$$f[MHz] = 0.1 \frac{\text{Beam Current}[nA]}{\text{Dose}[\mu C/cm^2] * \text{PixelSize}^2[\mu m]} \quad (5.1)$$

Exposure done, the resist is developed for 60 seconds in a developer solution of Mi-BK, Isopropanol in ratio 3:1, and then rinsed in isopropanol for additional 60 seconds.

The wafer is then dried with nitrogen gas. The resulting structure is shown in [e]. To ensure the absence of resist residual, descumming is performed by means of 20 seconds of oxygen plasma at 200 W in a Tepla GiGA-batch.



Figure 5.6: Ebeam resist development

The markers are then evaporated using the evaporator Leybold Optics LAB 600H; such evaporator is particularly indicated for lift off process having a maximum working distance of 1010 mm that allows to minimize the angle between the normal on the edge of a wafer and the incident flux of evaporated material, reducing the amount of metal deposited in side wall of the resist; leading to a smoother and easier lift-off process.

A first adhesion layer of 5nm of Titanium is evaporated and the actual markers are made by evaporating 55nm of Platinum or alternatively Palladium.



Figure 5.7: 5nm of Ti and 55nm of Pt or Pd are evaporated to form the markers

The wafer is then immersed in remover 1165 for 8 hours at 90°C and the lift offed layer is removed by pi-petting. The wafer is then cleaned in a bath of Methanol and ultrasonicated at frequency 80kHz and power 54W for 5 minutes. The cleaning process is then finalized by an additional rinsing in Isopropanol, ultrasonicated with the same parameters for 5 minutes; the wafer is then dried by means of a nitrogen gun and stored in a nitrogen cabinet.[g]

The following steps resulted to be the most critical in terms of stability and selectivity: the photo-lithography of the Aluminum ground plane.

Here will be reported the final, properly working recipes.



Figure 5.8: Resist stripping and lift-off

The wafer is firstly dehydrated for 5 min at 130°C, coated with a single layer of resist xxx, and soft-baked for x seconds at x temperature. The wafer is then exposed by means of a mask-less photo-lithography process, writing with a 405nm wavelength laser using the tool: Mask-Less Aligner, developed by Heidelberg Instruments GmbH.

Such exposure intended to pattern the following structure:

- readout coplanar waveguide (CPW) superconducting resonator
- frequency tuning flux line
- qubit state drive line
- transmission read out coplanar waveguide

as referenced in figure. The design is exposed with dose xxx and defocus yyy.



Figure 5.9: Photoresist coating

The resist must now be developed; to obtain the highest selectivity with respect to the Aluminum, the AZ developer has been used for xx seconds. Such step resulted to be particularly critical, infact all TMAH based developer tends to have a particularly high etching rate with respect to the Aluminum, which was resulted to be corroded during the developing process. But the adoption of the AZ developer diluted with deionized water in ratio 1:1, has shown good results in term of roughness, stability and repeatability, being non TMAH based. The wafer is than rinsed in deionized water and dried with nitrogen gun[i].



Figure 5.10: Photoresist exposure and development to define the ground plane.

The Aluminum is than etched with a solution of phosphoric and nitric acid; immersed in an overall volume of 250mL for 3 minutes and 15 seconds.

The wafer is than immersed in water to stop the etching process and rinsed in 3 deionized water bath. The wafer is than dried with nitrogen gun[i].



Figure 5.11: Aluminum wet etching

The resist is than stripped in a bath of remover 1165 for 5 hours at 90°C, and cleaned as described before in a standard process of ultrasonication at frequency 80kHz and power 54W, in methanol and isopropanol (IPA) bath. Before to process further the wafer is cleaned by plasma oxygen for 20 seconds at 200W [m].



Figure 5.12: resist stripping

The Niobium Nitride film must than be integrated in the Aluminum ground plane, only in the area dedicated to the metamaterial patterning; A second e-beam step is done:

wafer is thermally dehydrated at 180°C for 5 min and is coated by a double layer of MMA/PMMA to facilitate the sequent lift off; in details: a layer of MMA EL9 is spin coated at 1500 rpm to obtain a thickness of 500nm; the wafer is than soft-baked for 5min at 180°C. The second layer of resist is PMMA 495K A8 spin-coated at 4000 rpm to obtain

a resist thickness of 500nm; for a total resist thickness of $1\mu\text{m}$.

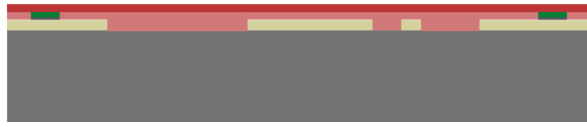


Figure 5.13: ebeam double layer coating for NbN deposition

The wafer is now loaded inside the e-beam system load-lock. Transferred in the exposure chamber the resist is exposed with a dose of 1450, a beam current of 100nA and a pixel size of 40nm. Exposure done, the resist is developed for 120 seconds in a developer solution of Mi-BK, Isopropanol in ratio 3:1, and then rinsed in isopropanol for additional 60 seconds.

The wafer is then dried with nitrogen gas. The resulting structure is shown in [o]. To ensure the absence of resist residual, descumming is performed by means of 20 seconds of oxygen plasma at 200 W in a Tepla GiGAbatch.

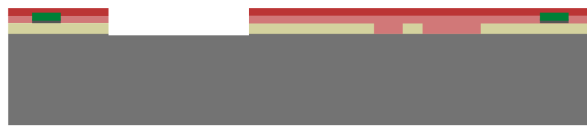


Figure 5.14: ebeam resist exposure and development

The high kinetic inductance Niobium Nitride (NbN) is then sputtered such to achieve a kinetic inductance of $90\text{pH}/\square$; this results in a 20nm film thickness.



Figure 5.15: NbN sputtering

The wafer is then bathed in remover 1165 for 8 hours at 90°C and the lifted-off layer is removed by pipetting. The wafer is then cleaned in a bath of Methanol and ultrasonicated at a frequency 80kHz and power 54W for 5 minutes. The cleaning process is then finalized by an additional rinsing in Isopropanol, ultrasonicated with the same parameters for 5 minutes; the wafer is then dried by means of a nitrogen gun and stored in a nitrogen cabinet.



Figure 5.16: NbN lift off

Once the NbN is sputtered the metamaterial must be patterned by e-beam lithography. The wafer is thermally dehydrated at 180°C for 5min and coated with CSAR C04 spin coated at 4000rpm. The resist is then soft-baked at 150°C for 5 min.

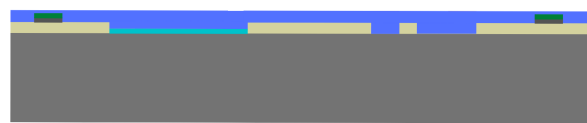


Figure 5.17: CSAR ebeam resist coating for metamaterial patterning

the patterning of the metamaterial was done by ebeam lithography; being the inductor 400nm wide, the feature has 100percent fill factor; this implies that the exposure must take into account for the back-scattering effect of electrons, electron proximity effect correction must be applied. The pattern is exposed with a pixel size of 10nm, a beam current of 5nA, a base dose of 190 with EPC parameters such that $\eta = 0.6$ and with an applied bias of -15nm.

Exposure completed, the resist is developed for 60 seconds in n-Amyl-Acetate and rinsed for additional 60 seconds in a solution of Mi-BK:IPA in ratio 90:10. The wafer is than dried with nitrogen gun.

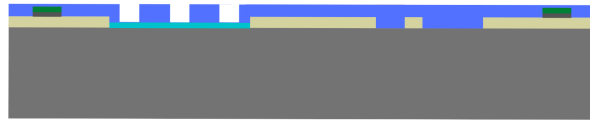


Figure 5.18: CSAR exposure and development

the NbN must be now dry etched to pattern the NbN metamaterial. The wafer is etched in a mixture of CF_4 and Ar for 11 minutes at 10W, after a prior chamber conditioning and cleaning with O_2 for 10 min.



Figure 5.19: Metamaterial dry etching

The resist is than stripped in a bath of remover 1165 for 48 hours at 90°C, and cleaned as described before in a standard process of ultrasonication at frequency 80kHz and power 54W, in methanol and isopropanol (IPA) bath.

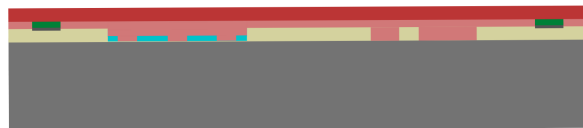


Figure 5.20: MMA/PMMA coating for SQUID junction patterning

The next step is the patterning of the SQUID junction, that as described before is composed as the parallel of two Josephson Junctions. The wafer is thermally dehydrated and coated with a double layer of MMA-PMMA: a layer of MMA EL9 is spin coated at 1500 rpm to obtain a thickness of 500nm; the wafer is than soft-baked for 5min at 180°C. The second layer of resist is PMMA 495K A8 spin-coated at 4000 rpm to obtain a resist thickness of 500nm; for a total resist thickness of 1 μ m.

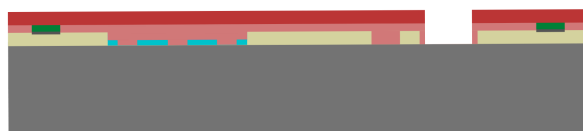


Figure 5.21: SQUID junction exposure and development

The wafer is now loaded inside the e-beam system load-lock. Transferred in the exposure chamber the resist is exposed with a dose of 1600, a beam current of 1nA and a pixel size of 2nm. Exposure done, the resist is developed for 120 seconds in a developer solution of Mi-BK, Isopropanol in ratio 3:1, and than rinsed in isopropanol for additional

60 seconds. The wafer is then dried with nitrogen gas. To ensure the absence of resist residual, descumming is performed by means of 20 seconds of oxygen plasma at 200 W in a Tepla GiGAbatch.

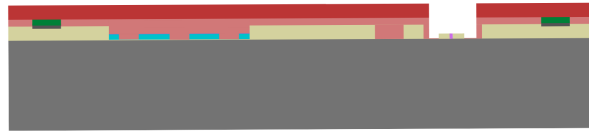


Figure 5.22: Plassys evaporation to form SQUID junction; one among Manhattan double angle, Manhattan triple angle, Dolan bridge technique are used

Patterned the junctions, the evaporation must be done at the UHV evaporator Plassys MEB550SL3; The wafer is loaded in the load-lock chamber and transferred to the evaporation chamber. Also in this case a shutter-close Titanium evaporation is performed such to form a layer of TiO_2 which absorbs the oxygen present inside the chamber. The arm moving the wafer holder inside the Plassys allows for tilting and rotation; this feature results to be fundamental for the following process: SQUID junction evaporation. Three main techniques can be found in literature to achieve the realization of Josephson junction through lift-off:

Manhattan evaporation (Double angle)

The Manhattan double angle evaporation consist in taking advantage of the resist thickness to mask the deposition along the direction perpendicular to the deposition. By referring to the schematic in figure, the wafer is tilted at 45° and a first layer of 35nm of Al is deposited along the single arm of the Junctions; noticing that the two parallel arms remains unaltered due to the shadowing effect of the double resist layer.

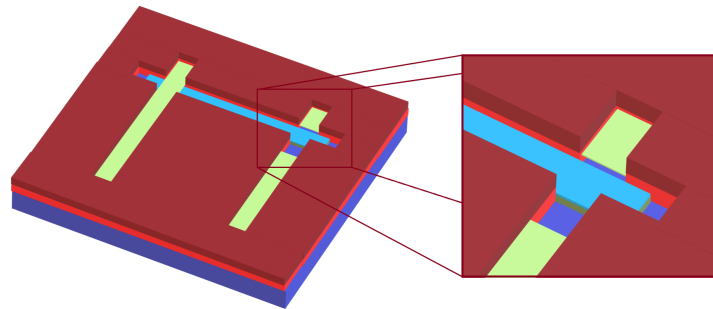


Figure 5.23: Schematic for the Manhattan evaporation of Josephson junction or SQUID junctions

The wafer is then transferred in the oxidation chamber, where a static oxidation is performed at 0.15 Torr for 4 minutes. The wafer is then transferred back to the evaporation chamber where a 90° rotation and 45° tilting is performed; the second evaporation is made along the two parallel arms of the SQUID junctions; noticing how this time the single arm remains untouched. At the end of the second evaporation, two Josephson Junctions (JJ) are formed at the intersection of the single arm and the two parallel arms. The wafer is now passivated in the oxidation chamber by growing a thick oxide for 10 min at 4 Torr.

Manhattan evaporation (Triple angle)

In the Manhattan triple angle evaporation, an additional 45° rotation and 45° tilting are added to the fabrication step. This, as will be more clear in the following, allow to directly patch the junctions to the Al ground plane, reducing an e-beam exposure, resulting in a cheaper process and in a reduction in the stress induced on the JJ.



Figure 5.24: Aluminum lift-off to define the Josephson junction

The wafer is then immersed in remover 1165 for 8 hours at 90°C and the lift offed layer is removed by pipetting. The wafer is then cleaned in a bath of Methanol and ultrasonicated at frequency 80kHz and power 54W for 5 minutes. The cleaning process is then finalized by an additional rinsing in Isopropanol, ultrasonicated with the same parameters for 5 minutes; the wafer is then dried by means of a nitrogen gun and stored in a nitrogen cabinet. [g]



Figure 5.25: ebeam resist coating for patching

The junction are now written, but electrically disconnected from the ground plane; a last e-beam lithography step is needed to patch the SQUID junctions. The wafer is thermally dehydrated and coated with a double layer of MMA-PMMA: a layer of MMA EL9 is spin coated at 1500 rpm to obtain a thickness of 500nm; the wafer is then soft baked for 5min at 180°C . The second layer of resist is PMMA 495K A8 spin-coated at 4000 rpm to obtain a resist thickness of 500nm; for a total resist thickness of $1\mu\text{m}$.

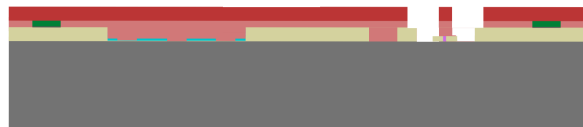


Figure 5.26: patch exposure and ebeam resist development

The wafer is now loaded inside the e-beam system load-lock. Transferred in the exposure chamber the resist is exposed with a dose of 1600, a beam current of 1nA and a pixel size of 2nm. Exposure done, the resist is developed for 120 seconds in a developer solution of Mi-BK, Isopropanol in ratio 3:1, and then rinsed in isopropanol for additional 60 seconds. The wafer is then dried with nitrogen gas. To ensure the absence of resist residual, descumming is performed by mean of 20 seconds of oxygen plasma at 200 W in a Tepla GiGAbatch.

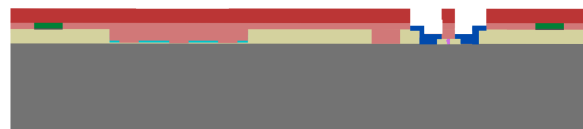


Figure 5.27: Aluminum evaporation to form the metallic contact.

The wafer is now loaded inside the plassys, a constant holder rotation is applied to ensure deposition uniformity and 200nm of Al are evaporated electrically connect the Junctions to the ground plane. A final passivation at 4 Torr for 10 minutes is then performed, forming a layer of AlO_3 covering the device surface.



Figure 5.28: Aluminum lift-off

The resist is then stripped in a bath of remover 1165 for 4 hours at 90°C, and cleaned as described before in a standard process of ultrasonication at frequency 80kHz and power 54W in methanol and isopropanol (IPA) bath.

[Dicing] The wafer is now coated with 1.2 μ m of photo-resist AZ 1512HS such to allow a mechanical protection during the dicing process. The wafer is then diced by means of the Disco DAD321, resulting in dies of 4cm height x 7cm wide. Finally the resist protecting the chips is stripped in remover 1165 at 95°C; chips are then cleaned in methanol and isopropanol, ready to be bonded in the PCB.

[Bonding] The chips are now manually bonded with Al wires to the PCB through a manual ultrasound bonder. The device is grounded and the signal lines are connected, as shown in the figure:

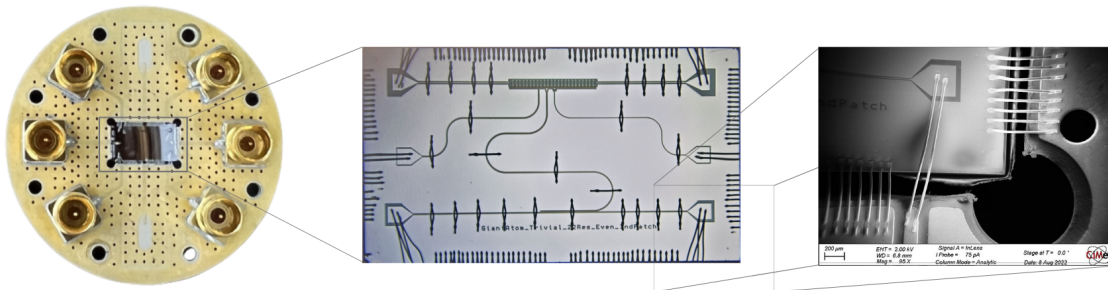


Figure 5.29: Final device mounted and bonded with Al wires on the PCB

[Final mounting and covering] After the bonding process, the chip looks as shown in figure; The PCB is screwed on a cooper mount and shielded with an Aluminum cap such to suppress any unwanted standing wave. The RF device is now ready to be inserted in the cryostate, cabled and measured. In the following chapter an overview of the wiring and the measurement setup is discussed.

6

Measurement set-up

6.1. Dry dilution cryostat

A $^3\text{He}/^4\text{He}$ dilution refrigerator is a cryogenic device which cooling power is provided by the heat of mixing Helium-3 and Helium-4 isotopes. Given a certain amount of liquid Helium, the simplest way to lower its temperature is by means of evaporation cooling technique, where Helium vapour is pumped away, cooling the gas by the works done in contrast with the inter-atomic forces that caused the helium to liquefy in the first place.[13] While the temperature drops, the equilibrium vapour pressure follows the same trend, and consequently the rate at which helium gas can be extracted from the liquid helium bath drops. This represents a fundamental limitation in the lowest achievable temperature by means of evaporation cooling. In order to reach temperature range from 0.6K to 0.01K, dilution



Figure 6.1: Blue-fors, dry dilution cryostat.

cooling technique is needed. Let's now consider a mixture of ^3He and ^4He . ^4He atoms are bosons, while ^3He atoms are fermions: as can be seen from the phase diagram of the mixture, at temperature below 0.87K the two liquids are immiscible over a wide composition range. For $T \rightarrow 0$, the ^3He concentration in the mixture tends to be $\approx 6\%$, while the concentrated phase becomes essentially pure ^3He . If the ratio of Helium-3 over Helium-4 decreased below the 6%, due to an increase of ^4He or decrease of ^3He by dilution, thus in order to restore the equilibrium concentration, ^3He atoms evaporate from the concentrated ^3He liquid, in an endothermic process that absorbed heat resulting in the cooling of the surrounding environment. Almost all the Helium-4 have condensed in the ground state, on the other side the Helium-3 atoms behave as if they were present alone, as a gas occupying the volume of the mixture [13]. The quasi gas of ^3He diffuses from the mixing chamber through a counter flow, where it is heated by a combination of heater and through an heat exchange with the down coming flow of ^3He in the mixing chamber. The pumped-off

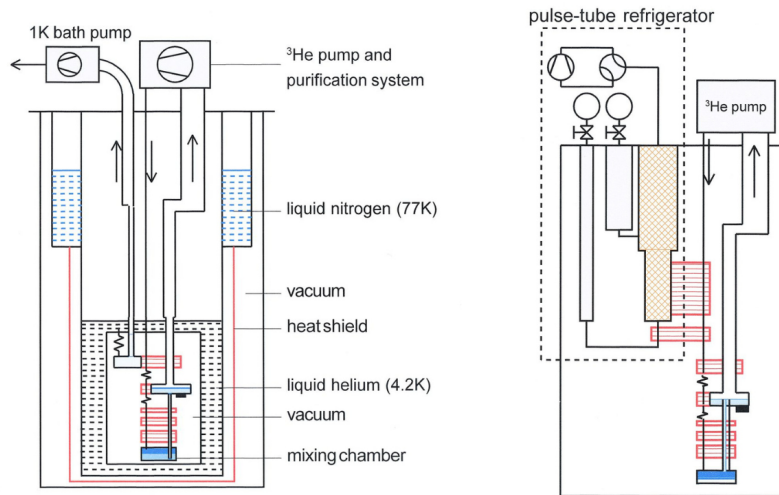


Figure 6.2: On the left, typical schematic of a wet dilution fridge, on the right schematic of a most recent pulse tube based dilution fridge.

^3He is then returned to the system and is condensed in a condenser that is cooled to about 1K by contact with a pumped (evaporation cooled) ^4He bath. The liquefied ^3He is cooled further, first in the still, then in the counter flow heat exchanger, before re-entering the mixing chamber.

6.2. Room temperature set-up

In the following section the main room temperature setup is presented; signal conversion technique and generators will be covered with a constant reference to the device wiring depicted in figure.

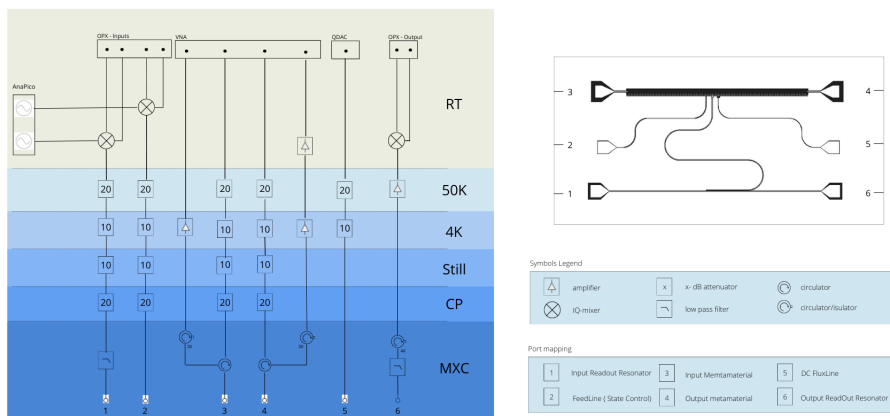


Figure 6.3: Wiring of the device and connection on the fridge; all the attenuation stage are shown at the different working temperature.

Most of the RF measurement are performed in a range of 3GHz - 12GHz; most of the standard RF setup, as amplifier and filter works in the spectrum, reason why most of the community choose to set qubit frequency in such interval.

6.2.1. IQ mixing

An extremely efficient way to generate signal in this spectrum is through the use of mixers and up/conversion signal processing techniques. The main idea behind so, is to mix a carrier signal generated by a local oscillator (LO) with

frequency ω_{LO} with an amplitude modulated signal (the one carrying the actual information) at an intermediate frequency ω_{IF} . Such a process is called signal up conversion, on the contrary when the signal frequency is reduced to be analyzed by standard electronic, is called down-conversion.

A simple mixer simply multiply the two signal at frequency ω_{IF} and ω_{LO} . The output signal is as follow:

$$S_{UP} = \cos(\omega_{LO}t) \cos(\omega_{IF}t) = \frac{1}{2} \cos[(\omega_{LO} + \omega_{IF})t] + \frac{1}{2} \cos[(\omega_{LO} - \omega_{IF})t] \quad (6.1)$$

This results in a double side band signal, up-converted at a frequency that span around the local oscillator frequency. Filtering out one of those side-band is particularly inconvenient, considering that the device are frequency tunable over a wide spectrum. To avoid this issue, IQ mixer have been used.

An IQ mixer basically works as the combination of two standard mixers: The local oscillator input of the two mixer are phase shifted of $\pi/2$ one each other, and the same happen for the intermediate frequency of both. The two intermediate frequency are said to be in quadrature and they respectively input the IQ mixer in I and Q port. The output of those two virtual mixer is added up together resulting in:

$$S_{UP} = \cos(\omega_{LO}t) \cos(\omega_{IF}t) = \frac{1}{2} \cos[(\omega_{LO} + \omega_I)t] + \frac{1}{2} \cos[(\omega_{LO} - \omega_I)t] + \frac{1}{2} \sin[(\omega_{LO} + \omega_Q)t] + \frac{1}{2} \sin[(\omega_{LO} - \omega_Q)t] \quad (6.2)$$

where I and Q are the modulated signals generated in quadrature such that $\cos(\omega_q) = \sin(\omega_I)$ and the up-converted signal become:

$$S_{UP} = \frac{1}{2} \cos[(\omega_{LO} - \omega_I)t] \quad (6.3)$$

which, as wanted, is a single side band signal

Vector network analyzer The vector network analyzer (VNA) generate RF signals and monitor the systems response. In particular is able to generate and read out signal in a spectrum of 100 kHz up to 20 GHz, measuring not only the amplitude response but also the phase; this allows to efficiently measure the DUT both in transmission and reflection, for full device characterization.

Room temperature amplifier In order to amplify the signal generated in the cryostat, room temperature amplified are used at the output of the fridge, amplifying the signal of 30 db, considerably improving the signal to noise ratio.

Filters In order to filter the noise injected in the device and clean the output response, low pass filter are connected with a cut-off frequency of 8 GHz;

Attenuators In order to work in single photon regime and eliminate the thermal noise affected photons, a set of attenuator is added in the signal chain toward the device in the cryostat. In every of the shield, an attenuation stage is inserted and shown in the figure.

Anapico The local oscillator signal, described in the IQ mixing section, is generated by the Anapico RF signal generator.

OPX The Quantum Machine OPX is an extremely efficient signal generator that allow to precisely send time domain signals with a time scale of:

7

Experimental results

7.1. Time of Flight

First fundamental step is the IQ mixers calibration; The delay of the signal travelling along the coaxial cables must be compensated by performing a standard time of flight measurement and adjusting the offset between the two I-Q quadrature.

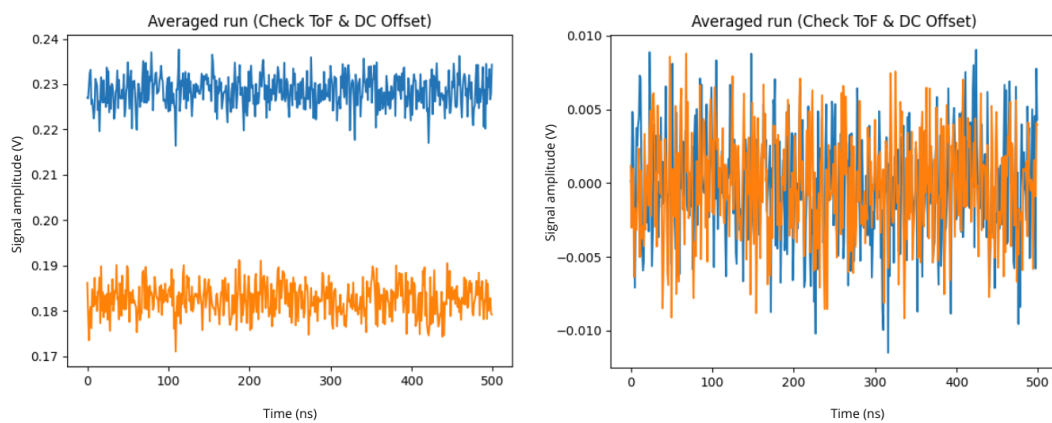


Figure 7.1: On the left, uncalibrated signal; on the right signal after correction

7.2. Read out resonator characterization

Once the IQ mixer are calibrated and ready to use, the device can start to be spectroscopically characterized. The first fundamental element to be investigated is the correct functioning of the read out resonator. As previously explained, such resonator is on a hanged configuration, inductively coupled to the signal feed line.

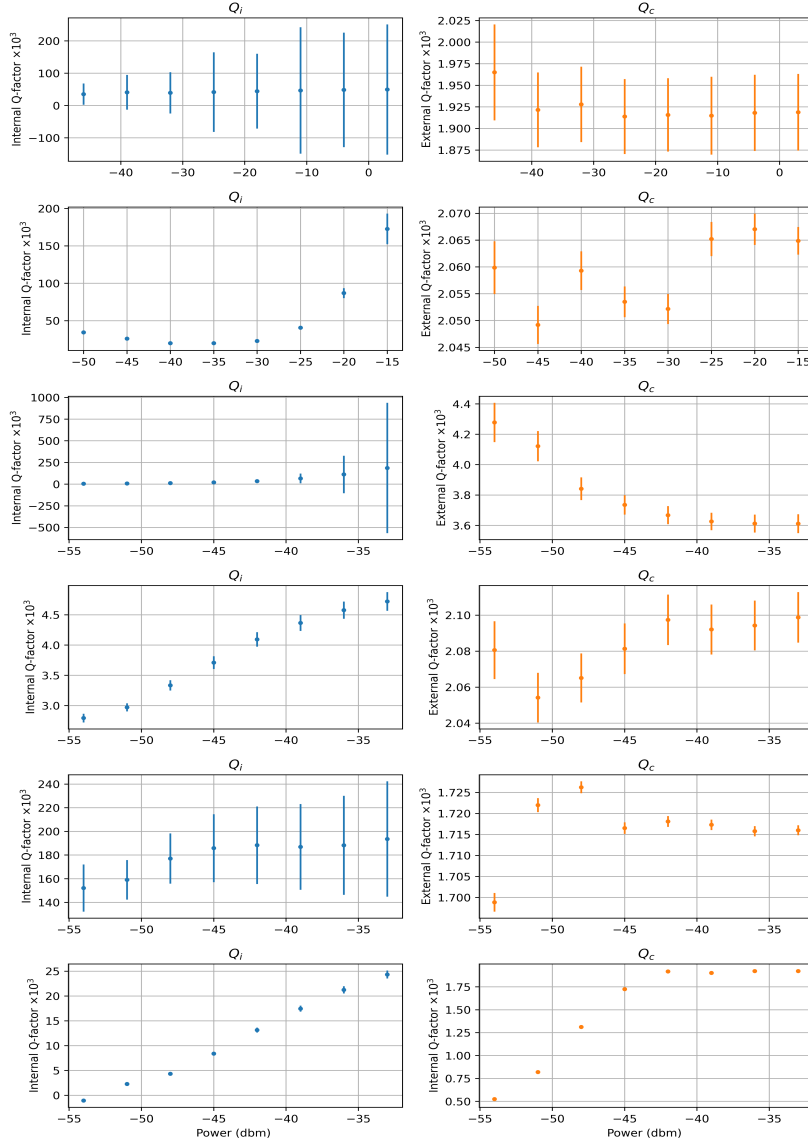


Figure 7.2: Read out resonator quality factor for different tested fabrications

Through the VNA a signal is emitted in the input of the feed line ranging a frequency spectrum of approximately 1GHz around the designed read out resonator resonance frequency; the measurement of the complex coefficient S_{21} should result in a dip in correspondence of the resonance frequency ω_r . The full width half maximum of such dip, corresponds to the photon decay rate, by means of which is possible to extract the resonator quality factor as:

$$Q = \omega_r / \kappa \quad (7.1)$$

which in this case resulted to be up to 190000 for the internal quality factor of the 5th fabrication.

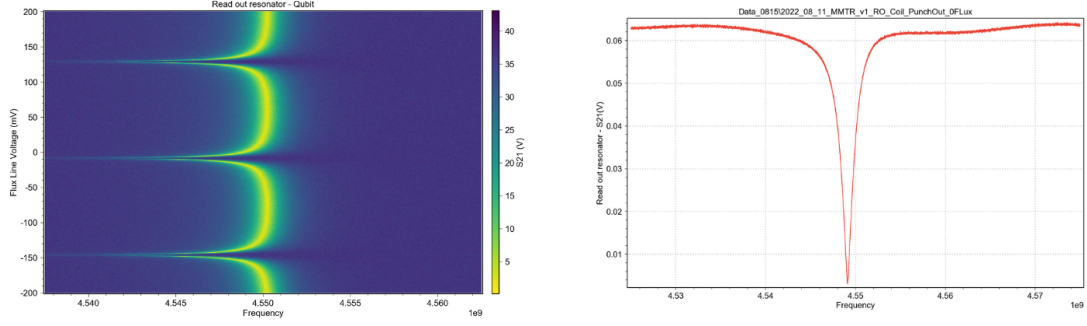


Figure 7.3: on the left, read out resonator coupling to transmon qubit, on the right, read out resonator hanged configuration resonance peak.

7.3. Punch out

The next set of measurement wants to allow for a firstly basic understanding of the qubit state. In order to understand whether the qubit is alive or not, so called punch out is performed. Being the qubit coupled to the read out resonator, the overall hybridised system is slightly non linear, thus, to detected the qubit presence it sufficient to stimulate the cavity by an increasing power signal over a frequency range centered around the readout resonator resonance frequency. As already seen previously, the Janes cunning Hamiltonian describing the qubit cavity interaction is in the form:

$$\hat{H} = \omega_r(\hat{a}^\dagger \hat{a} + \frac{1}{2}) - \frac{\omega_q}{2} - g(\hat{a}^\dagger \sigma_- + \hat{a} \sigma_+) \quad (7.2)$$

where $\hat{a}^\dagger \hat{a} = \hat{n}$ is the photon number operator, such that:

$$\hat{n} |\psi_n\rangle = n |\psi_n\rangle \quad (7.3)$$

in other word, is the operator that applied to the n-th eigenfunction, it return the number of photons in that mode. On the other side the coupling term of the Hamiltonian is proportional to \sqrt{n} . A power increase correspond in general to a increase of photons injection in the system, which lead the resonator term in the Hamiltonian dominated over the coupling term when $n > \sqrt{n}$.

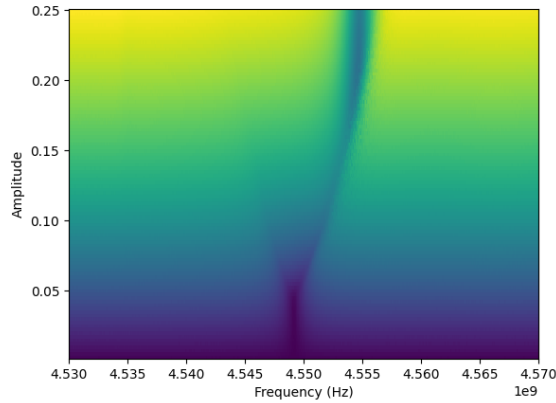


Figure 7.4: Resonator punch out

In such situation the system respond by shifting the overall resonance frequency stabilizing around the resonator bare frequency. Additional information can be extracted from this preliminary measurement; if the high power frequency shifts to a lower frequency, the qubit frequency is located below the cavity and vice versa. A bigger shift means that the cavity and the qubit are more strongly coupled. [16]. If qubit and resonator are not far detuned: $\Delta < g$, the two systems enter the polariton regime and two distinct peaks can be observed, spaced by $\approx 2g$.

7.4. Multi-mode environment

The multimode system is measured by detecting the power spectrum transmission through the metamaterial. For different configuration, a certain engineered spectrum is expected to be measured, with a total number of modes equal to the number of physical resonator on the coupled cavity array. The modes distribution differs for different working regime, among normal, trivial and topological configuration.

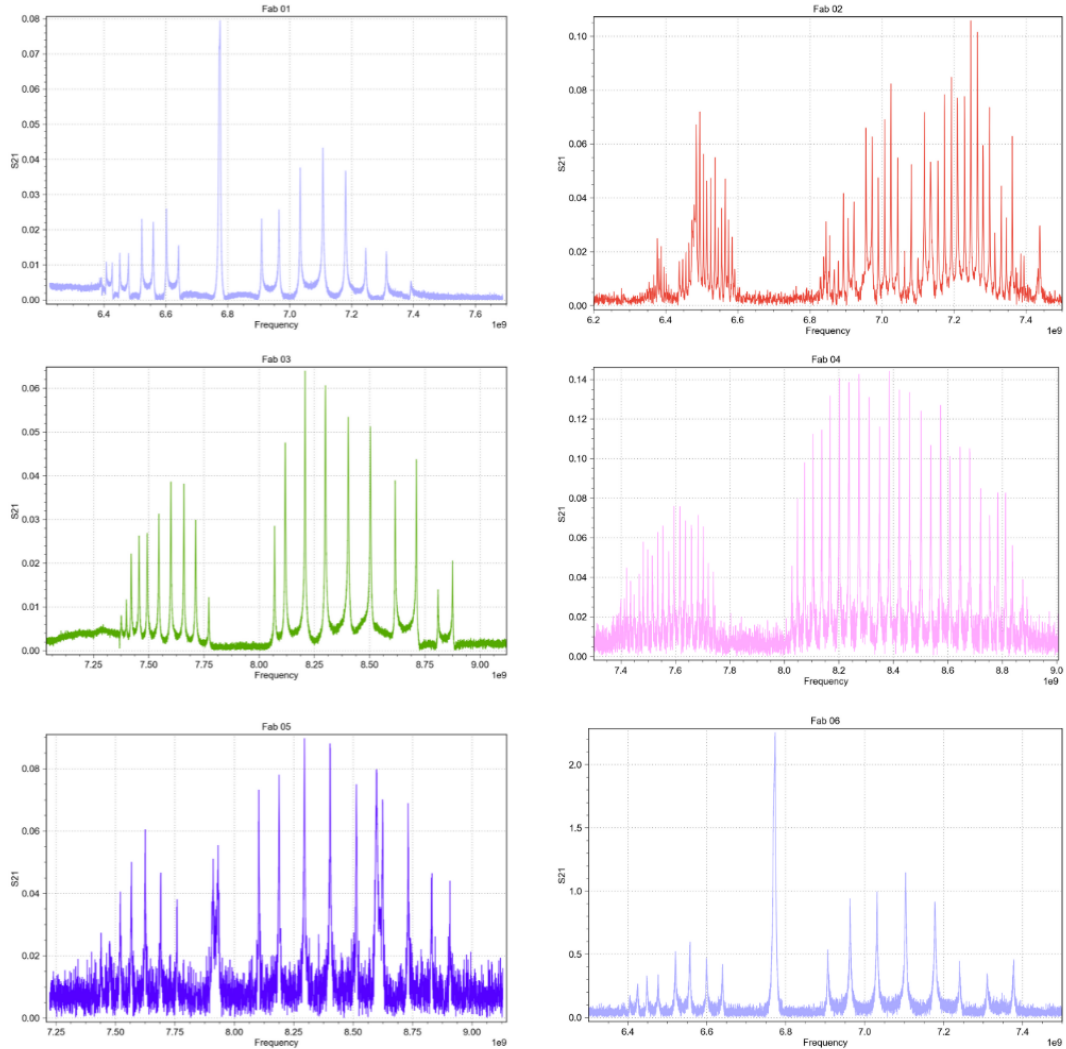


Figure 7.5: Metamaterial spectrum $|S_{21}|^2$ for different fabrications

It's importance to remember that the superconducting metamaterial was made out of a concatenation of lumped high impedance resonator. The quality factor and hence the coherence time for the each of modes are not expected to be relevantly high, indeed the main targets are on side the coupling between the metamaterial and the small electric dipole moment of the transmon qubit, on the others, the possibility to achieve ultra compact metamaterial resonator to enable scalability of high number of modes system, leads in an implementation based on disordered high kinetic inductance superconductor as NbN with much inferior quality factor with respect to pure Al metamaterials.

7.5. Transmon coupled to metamaterial

Two tones spectroscopy has demonstrate the qubit to be "alive", responding to driving signal and flux tunable. The next experiment consist in the spectroscopic analysis of the metamaterial transmon interaction; in order to so the qubit has to be flux tuned in the multi mode system spectrum. The extreme sensitivity of Josephson junction to process parameters fluctuation leaded the qubit 0-flux frequency to be slightly higher than the designed one; this results in the need of strongly flux tuning the device leading to high sensitivity to flux noise, charge noise and a decrease in anharmonicity. Nonetheless the experiment has been successfully finalized, interacting with a metamaterial in topological configuration.

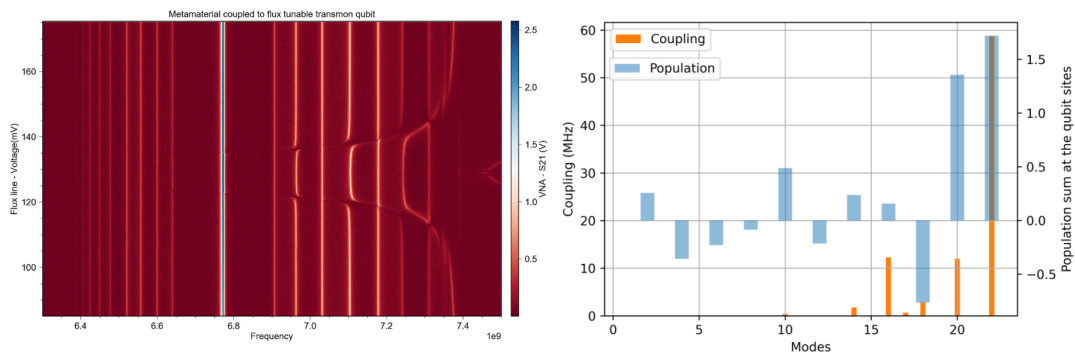


Figure 7.6: Weighted sum of photon distribution for a qubit coupled to N cavities in the metamaterial.

The transmon is coupled to multiple points of the metamaterial, in particular from cavity 7 to 16. Flux tuning leads to a decrease in the JJ critical current, inductance increase and consequent frequency decreasing. The transmon approaches firstly the band edge modes, resulting in what looks to be atom photon bound state, As can be seen from the Fig Fig 7.6(right) the net photon population in the correspondence of the physical qubit location changes depending on which modes the system is driven; In the high frequency band the photon population result to be much higher than the lower band, following a trend of alternate photon number distribution. This result in having strongly coupling with those modes where the photon distribution is the highest. Experimentally this has been observed as avoided crossing at alternate modes as can be seen from Fig 7.6(left) As can be seen, the transmon couples much stronger to the upper band edge than the lower one; this can be intuitively seen by referring to Fig. 3.4: The eigenstates in the lower band modes have an anti-symmetric photon distribution, which lead to their interaction "cancelling out" resulting in weak coupling, in opposition to the symmetric eigenstate distribution for the upper band modes to which strong coupling is observed.

7.6. Two tones spectroscopy

Once the qubit is demonstrated to be "alive", now its resonance frequency must be found; to do so, two tones spectroscopy measurement is performed. The idea is following:

A continuous microwave signal S_1 is sent and maintained at the exact low power cavity resonance; being the read out resonator in hanged configuration to the bottom feed line, all the photon injected in the waveguide are absorbed by the resonator and this will results in an signal absence when measuring at feed line output.

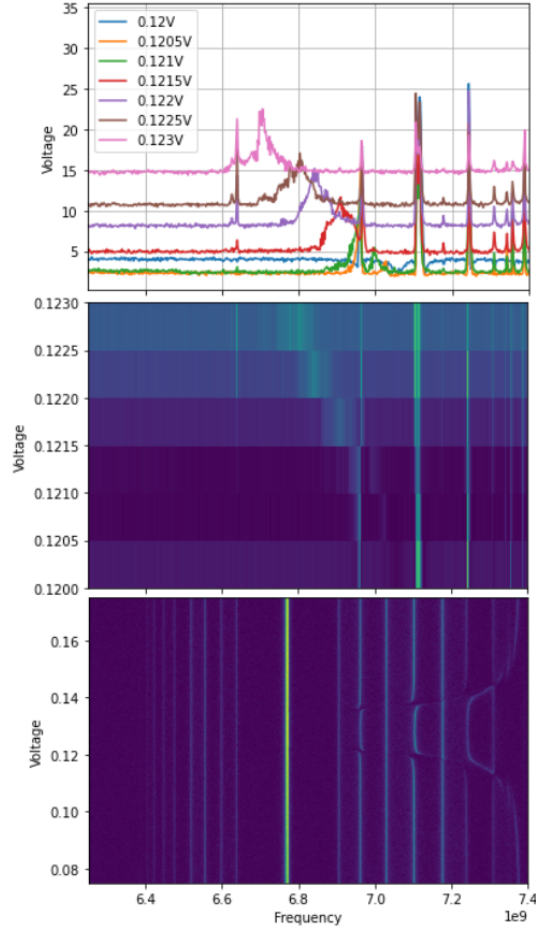


Figure 7.7: Two tones spectroscopy measurement; from the top: full metamaterial spectrum, two tones color map and two tones 2D graph for different applied magnetic fields.

While the first signal is on, another microwave signal (S_2) is sent through the state control line, sweeping the frequency of the least. Once the control line signal match the resonance frequency of the qubit ω_q , it get excited moving on average from its ground state. As previously explained, the qubit excitation from its eigenstate $|0\rangle \rightarrow |1\rangle$, leads a shift of the resonance frequency of the read out resonator coupled to it. Now, because the signal S_1 does not matched anymore the low power read out resonator frequency, the transmitted power measured from the feed line output increase its value. By further increasing the signal S_2 power, multi photon excitation occurs, detecting the resonance frequency of the transition between first and second excited state, resulting in a second peak at lower frequency. By means of simply measuring the distance between the two peaks, the transmon anharmonicity is derived as $\omega_{eg} - \omega_{fe}$. In this measurement it has been possible to spectroscopically observe the metamaterial modes to which the transmon was more strongly coupled, being those the artificial atom is most likely to exchange energy with. This is perfectly coherent with the experimental result showed in Fig. 7.6

8

Conclusion

This thesis has shown the realization of a device for simulating the coupling among an artificial two level system and a structured multi-mode bosonic environment.

A microwave metamaterial, made out of a dimerized chain of LC high impedance resonator has been realized, aiming to behave as a photonic bath with engineerable dispersion relation. A frequency tunable transmon qubit has been coupled to multiple site of it, leading to the experimental realization of a platform for multimode coupling. The coupled system exhibits atom photon bound state behaviour in the vicinity of the band edge of the metamaterial spectrum.

The system Hamiltonian's has been modeled for different configurations and the device has been designed through the python library gdsSpy, simulated with the FEM software Ansys and Sonnet.

Five fabrications runs have been completed to efficiently combine type 1 superconductor (Aluminum), and type 2 superconductor (Niobium Nitride). The high kinetic inductance of NbN on one hand allowed to obtain ultra compact resonators and metamaterial and on the other hand allowed to obtain strong atom-photon coupling given by the high impedance resonators. Aluminum allowed instead to obtain high quality factor CPW resonator, and magnetic flux insensitive transmon qubit.

The most critical component resulted to be the SQUID junction; the fabrication of it required numerous tests and calibrations due to the high process variation sensitivity of the thin oxide layer.

Nonetheless the strong coupling among the bosonic environment and the transmon qubit has been shown at high flux tunability, allowing for a complete spectroscopic characterisation of the system. The strong magnetic applied magnetic field led the critical current of the junction to decrease in such way that the Josephson energy E_j became comparable to the charging energy E_C , leading to extremely sensitivity to charge and flux noise. Due to this the system has not been studied in time domain.

In the future, it is planned to further expand this platform by optimizing the junction fabrication. Due to the compact size and the high impedance of the resonators, it is aimed to explore atom-photon bound states in the multimode ultra-strong coupling regime [18], as well as the giant-atom regime [1]. Furthermore, it is also planned to study the interactions between atom-photon bound states in 2D metamaterial [10].

References

- [1] Gustav Andersson et al. “Non-exponential decay of a giant artificial atom”. In: *Nature Physics* 15.11 (2019), pp. 1123–1127.
- [2] Frank Arute et al. “Quantum Supremacy using a Programmable Superconducting Processor”. In: *Nature* 574 (2019), pp. 505–510. URL: <https://www.nature.com/articles/s41586-019-1666-5>.
- [3] Já nos K. Asbóth, László Oroszlány, and András Pályi. *A Short Course on Topological Insulators*. Springer International Publishing, 2016. DOI: 10.1007/978-3-319-25607-8. URL: <https://doi.org/10.1007%2F978-3-319-25607-8>.
- [4] G. Aviv. “SQUIDS-Superconducting Quantum Interference Devices”. In: 2008.
- [5] Amgalanbaatar Baldansuren. “Small Ag clusters supported on an LTA zeolite investigated by CW and pulse EPR spectroscopy, XAS and SQUID magnetometry”. In: 2009.
- [6] Lucas Casparis et al. “Superconducting gatemon qubit based on a proximitized two-dimensional electron gas”. In: *Nature Nanotechnology* 13.10 (July 2018), pp. 915–919. DOI: 10.1038/s41565-018-0207-y. URL: <https://doi.org/10.1038%2Fs41565-018-0207-y>.
- [7] R Feynman. “Simulating physics with computers”. In: *J. Theor. Phys* 21 (1982), pp. 467–488.
- [8] Anton Frisk Kockum. “Quantum Optics with Giant Atomsthe First Five Years”. In: Jan. 2021, pp. 125–146. ISBN: 978-981-15-5190-1. DOI: 10.1007/978-981-15-5191-8_12.
- [9] Anton Frisk Kockum, Per Delsing, and Göran Johansson. “Designing frequency-dependent relaxation rates and Lamb shift for a giant artificial atom”. In: *Physical Review A* 90 (June 2014). DOI: 10.1103/PhysRevA.90.013837.
- [10] Alejandro González-Tudela and Fernando Galve. “Anisotropic quantum emitter interactions in two-dimensional photonic-crystal baths”. In: *ACS Photonics* 6.1 (2018), pp. 221–229.
- [11] Andrew A. Houck, Hakan E. Türeci, and Jens Koch. “On-chip quantum simulation with superconducting circuits”. In: *Nature Physics* 8.4 (2012). Using a well-controlled quantum system to simulate complex quantum matter is an idea that has been around for 30 years and put into practice in systems of ultracold atoms for more than a decade. Much recent excitement has focused on a new implementation of quantum simulators using superconducting circuits, where conventional microchip fabrication can be used to take design concepts to experimental reality, quickly and flexibly. Because the quantum particles in these simulators are circuit excitations rather than physical particles subject to conservation laws, superconducting simulators provide a complement to ultracold atoms by naturally accessing non-equilibrium physics. Here, we review the recent wealth of theoretical explorations and experimental prospects of realizing these new devices., 292–299. ISSN: 17452473. DOI: 10.1038/nphys2251. URL: <http://dx.doi.org/10.1038/nphys2251>.
- [12] Eunjong Kim et al. “Quantum electrodynamics in a topological waveguide”. In: *Physical Review X* 11.1 (2021), p. 011015.
- [13] C. Kittel et al. *Thermal Physics*. W. H. Freeman, 1980. ISBN: 9780716710882. URL: <https://books.google.ch/books?id=c0R79ny0oNMC>.
- [14] Philip Krantz et al. “A quantum engineer’s guide to superconducting qubits”. In: *Applied Physics Reviews* (2019).
- [15] Sebastian Krinner et al. “Realizing repeated quantum error correction in a distance-three surface code”. In: *Nature* 605.7911 (2022), pp. 669–674.
- [16] Mahdi Naghiloo. “Introduction to Experimental Quantum Measurement with Superconducting Qubits”. In: *arXiv: Quantum Physics* (2019).
- [17] RK Naik et al. “Random access quantum information processors using multimode circuit quantum electrodynamics”. In: *Nature communications* 8.1 (2017), pp. 1–7.

-
- [18] Thomas Niemczyk et al. “Circuit quantum electrodynamics in the ultrastrong-coupling regime”. In: *Nature Physics* 6.10 (2010), pp. 772–776.
- [19] David Isaac Schuster. “Circuit quantum electrodynamics”. PhD thesis. Yale University, Connecticut, Jan. 2007.
- [20] Marco Scigliuzzo et al. “Extensible quantum simulation architecture based on atom-photon bound states in an array of high-impedance resonators”. In: *arXiv preprint arXiv:2107.06852* (2021).
- [21] W. P. Su, J. R. Schrieffer, and A. J. Heeger. “Solitons in Polyacetylene”. In: *Phys. Rev. Lett.* 42 (25 June 1979), pp. 1698–1701. DOI: 10.1103/PhysRevLett.42.1698. URL: <https://link.aps.org/doi/10.1103/PhysRevLett.42.1698>.
- [22] Neereja M. Sundaresan et al. “Interacting Qubit-Photon Bound States with Superconducting Circuits”. In: *Phys. Rev. X* 9 (1 Feb. 2019), p. 011021. DOI: 10.1103/PhysRevX.9.011021. URL: <https://link.aps.org/doi/10.1103/PhysRevX.9.011021>.
- [23] V.J Weibel. “Microwave Superconducting Metamaterial for Analog Quantum Simulation”. 2021.
- [24] Xueyue Zhang et al. “A scalable superconducting quantum simulator with long-range connectivity based on a photonic bandgap metamaterial”. In: *arXiv preprint arXiv:2206.12803* (2022).
- [25] G. Zheng. “Circuit Quantum Electrodynamics with Single Electron Spins in Silicon.” PhD thesis. 2021.